

# A Compression-Loaded Double Lap Shear Test: Part 1, Theory

D.-A. Mendels, S.A. Page, J.-A. E. Månson  
Laboratoire de Technologie des Composites et Polymères (LTC)  
Ecole Polytechnique Fédérale de Lausanne (EPFL)

J.A. Nairn  
Material Science & Engineering Department, University of Utah  
Salt Lake City, UT USA

**Abstract** — This paper introduces a new approach to adhesion tests by a compression-loaded, double lap shear specimen and presents stress analysis of that specimen. The geometry modifies conventional double lap shear tests to minimize peel stresses and facilitate specimen fabrication, and thereby increase test reproducibility. The bonded part of the new specimen is identical to a conventional double lap shear specimen, but the specimen is end-loaded in compression instead of in tension. We analyzed the stress state using a new shear-lag theory for multilayered systems that includes residual stresses and friction on debonded surfaces. Axial stresses, shear stresses, and axial displacements were calculated for specimens stressed in the elastic regime, or beyond where local damage or yielding of the adhesive are present. They all compared well with the results of finite element analysis. Failure models of the specimen were derived using both strength and energy release rate methods. The model captured all the essential features of the energy release rate, including the effects of internal stresses and of friction at the debonded interface, within a certain range of debond length and friction stress. The results in this paper will be used in the remaining articles of this series, demonstrating the effects of internal stresses and physical aging of the adhesive on practical adhesion.

## 1. Introduction

Advanced composite materials are widely used in applications in the aircraft and automotive industry due to their high strength-to-stiffness ratio and high corrosion resistance. Their use as structural materials often requires the polymer-based composite to be attached to another structure, by means of bolted joints or an adhesive layer. An advantage of an adhesive layer is that it can limit stress concentrations due to bolts [1, 2].

A bonded adhesive structure consists of three components of different mechanical properties, namely the two adherents and the adhesive layer. Much attention has been paid to describing the mechanical response of such assembled systems, including their behavior under bending [3], tension, and shear [4, 5]. The bending and tension tests of joints generally involve mixed modes of failures with unknown shear components [6]. In order to predict failure in a non-trivial geometry, it is of primary importance to determine the characteristics of shear failure alone, which is the subject of the present series. The problem of shear failure of interfaces is relevant to several applications, such as metal to polymer composite bonding, metal to metal brazing, and composite interlaminar failure [7].

Adhesive failure is generally modelled by one of four approaches, namely:

- a shear strength criterion [8, 9, 10, 11];
- a local shear strain criterion [13];
- a fracture mechanics approach, using either the stress intensity factor [14, 15], or the energy release rate [16].

All these methods rely first on determination of the stresses in the system. Because of the complexity of the multi-material geometry, however, an exact analytical treatment of stress is not possible [17]. All analytical models, therefore have used simplifying assumptions [18]. Alternatively, numerical methods, including finite element (FEA) and boundary element analyzes (BEA), have been used [13, 19, 20, 21]. Due to specific

limitations of FEA at interfaces, it is not possible to treat all three components of an adhesively bonded structure as an elastic continua, and the problem is generally handled by using interface elements or by averaging stresses over a region close to the interface.

The primary factors influencing the choice of stress-analysis approximations are the adhesive-to-adherent(s) thickness ratios, and the ratio of the adherent thickness to the lateral joint dimensions [10, 11]. Most analytical models stem from the classical theory of beams or plates and shells [18]. These usually consist of first-order approximations of displacements, which, however, are incompatible with high deformations. In addition, these approximations neglect free-edge effects, although some asymptotic methods have been used in homogenizing these solutions to satisfy most boundary conditions [22, 23, 24]. The failure of an adhesive joint is not a property of the adhesive alone, but is a system property depending on adherents, the adhesive, the joint geometry, preparation, and service (or test) conditions [25]. The most widely used test methods are the general lap-shear tests. Early attempts, including those by Volkersen [10] or Goland and Reissner [11], to describe the stress field in simple lap-shear geometry, consisting of two plates bonded by a glue film, have led to inaccurate results essentially due to the existence of a peel stress generated by flexure of the adherents due to misalignment. Its magnitude, as well as the geometry variations between samples, was found to strongly reduce the reliability of the test results [12]. It is difficult to manufacture specimens with a controlled bond thickness without leaving spacers inside the joint. The effects of a glue meniscus [14] and the initial stress state [9, 16] on the strength of the adhesive bond are generally ignored. Furthermore, internal stresses, such as thermal residual stresses, have been shown to play an important role in adhesive performance [26, 27], but their effect has not been studied directly in lap joints. Moreover, several experiments have shown the need to account for local variations in the adhesive mechanical behavior. This includes possible damage to the adhesive, such as local interfacial debonding [28] or transverse cracking [29], and other effects such as viscoelasticity and plasticity [30].

In order to study the above effects, a new lap-shear test geometry, which allows specimen preparation difficulties to be minimized and takes into account the development of complex stress states, is introduced. The proposed modified double lap shear (MDLS) specimen enables tight control of the thickness of the adhesive layers with sharp edges, and introduces the possibility of moulding several samples at the same time, with virtually identical boundary conditions and thermal history. The stress state in the MDLS specimen, including residual stresses, was calculated here using a recent shear-lag method [39]. This theory was extended to account for non-perfect interfaces and also local variations in the adhesive mechanical behavior. Two alternative methods are used to interpret failure properties of lap joints, namely the interfacial shear strength approach and the fracture mechanics or energy release rate (ERR) approach. While the strength approach is straightforward once the local stress state is known, the ERR approach requires further calculations. First, an exact expression of the energy release rate was obtained by adapting results for a general composite geometry [16] to that of the MDLS specimen. After some minor approximations, this expression gave the energy release rate in terms of only axial stresses and displacements. Inserting the shear-lag results for these terms led to an approximate, analytical result for ERR. The local stress state and the approximate energy release rate compared well to FEA results. The theory developed in this article will be used in subsequent papers to analyze the results of:

- local strain mapping experiments [31];
- experiments where the internal stress state of the adhesive was tailored by modifying the cure cycle or by adding a chemical modifier to the adhesive [32];
- experiments where the mechanical behavior and internal stress state of the adhesive were changed by aging at temperatures below the glass transition temperature of the adhesive [33];
- interfacial crack propagation in laminates subjected to static or cyclic loading [34].

## 2. Problems Addressed and Associated System Geometry

Experimental results [31–34] show that loading of a modified double lap shear specimen (MDLS) leads to several damage modes which necessitates several model geometries for analysis. Fig. 1 presents the geometry for a MDLS specimen with cracks of length  $a$  between the adhesive layer and the central adherent. The

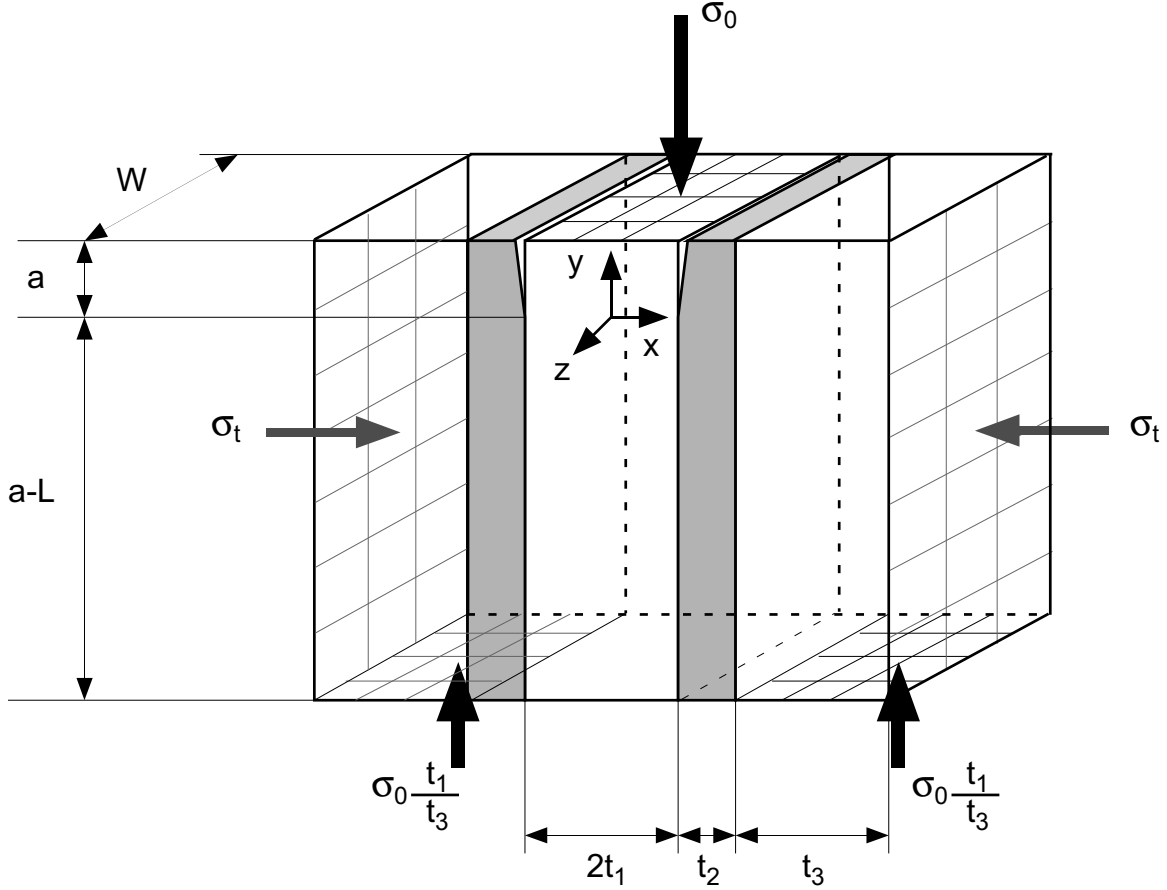


Fig. 1. Geometry of the modified double lap-shear specimen with cracks of length  $a$  between the adhesive and the central adherent layer.

system is shown with 3 constituents: an inner plate of thickness  $2t_1$ , with Young's modulus  $E_1$ , Poisson's ratio  $\nu_1$ , and thermal expansion coefficient  $\alpha_1$ ; two adhesive layers of thickness  $t_2$  and thermo-elastic properties  $E_2$ ,  $\nu_2$ ,  $\alpha_2$ ; and two outer plates of thickness  $t_3$  and thermo-elastic properties  $E_3$ ,  $\nu_3$ ,  $\alpha_3$ . The boundary conditions are defined by a compression stress of positive magnitude  $\sigma_0$  spread over the entire inner plate while the two outer plates are simply supported. The top and bottom surfaces of the adhesive layer are not loaded or supported. Additionally, two lateral pressures ( $\sigma_t$ ) can be applied on the outer adherents. The origin of the  $(x, y, z)$  axis system is in the middle of the specimen and aligned with the crack tip. The  $x$  axis is in the thickness direction while the  $y$  axis is in the loading direction.

The specimen geometry is symmetrical about the midplane, which means only half the specimen needs to be analyzed (see Fig. 2). The inner plate is labeled 1, the adhesive layer 2, and the outer plate 3. The width of the specimen  $W$  is assumed large enough to be in plane stress conditions in the  $z = 0$  plane of the specimen. This will be verified in the experimental part of this work by examining the fracture surfaces of the specimen [32–34]. The shear-lag analysis consists of determining the three averaged axial stresses  $\langle \sigma_{yy}^{(1)} \rangle$ ,  $\langle \sigma_{yy}^{(2)} \rangle$ ,  $\langle \sigma_{yy}^{(3)} \rangle$  in the layers, and the interfacial shear stresses  $\tau_{xy}^{(1)}$  (at the layer 1/layer 2 interface),  $\tau_{xy}^{(2)}$  (at the layer 2/layer 3 interface). The shear stress at the midplane ( $\tau_{xy}^{(0)}$ ) and on the lateral surface ( $\tau_{xy}^{(3)}$ ) are zero by symmetry or by boundary conditions. The calculation of the energy release rate required determination of the average displacements in the  $y$  direction  $\langle v^{(i)} \rangle$  in the system. These could also be found by the shear-lag analysis.

From experimental results [31–34], it was determined that four problems need to be addressed: i. the

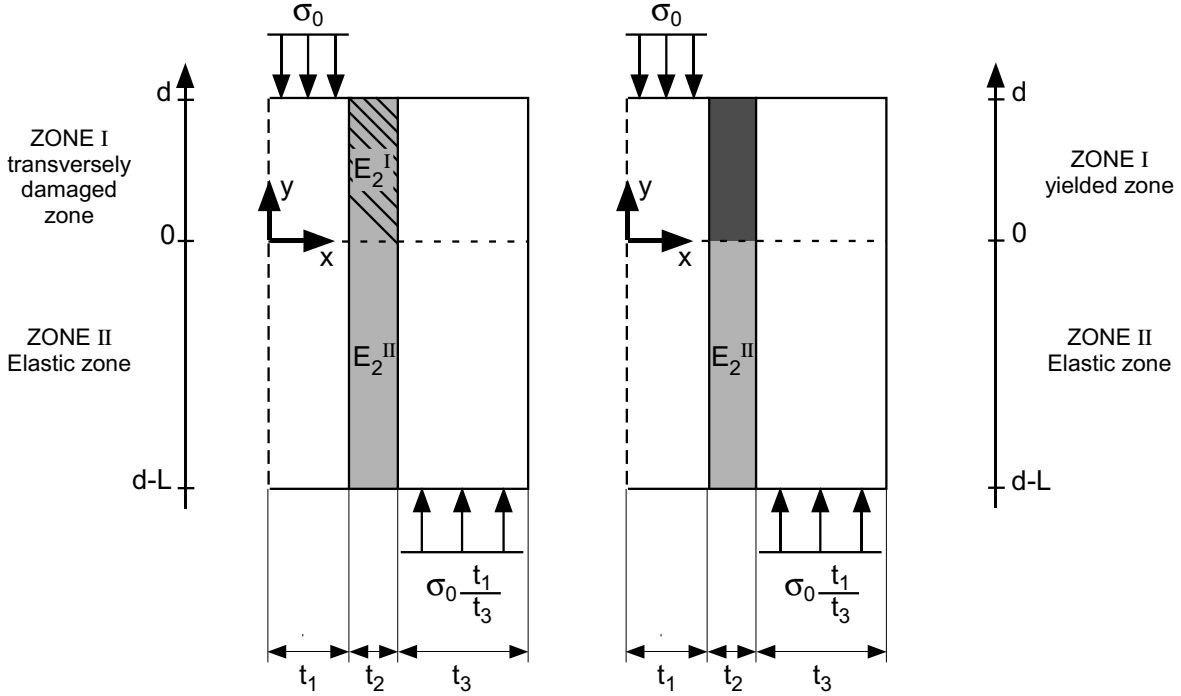


Fig. 2. Geometry of the MDLS specimen with a damaged zone of length  $d$  in the adhesive and 2 zones ( $I$  and  $II$ ) for the analysis. The damage zone can be a transversely cracked adhesive or a yielded adhesive

specimen fails in the elastic regime, ii. the adhesive mechanical properties are degraded locally prior to failure, iii. the adhesive partially yields prior to adhesive failure, and iv. a crack propagates at the interface between the inner plate and the adhesive. The first problem can be solved by a strength analysis using the shear-lag analysis. The three others are complicated if all local dissipative phenomena are to be accounted for. Instead, we used a global approach: the properties of a transversely damaged zone or of a yielded zone were averaged over the damage or yield length  $d$  (Fig. 2).

The two problems shown in Fig. 2 are very similar when a global approach is used. They both necessitate the introduction of two zones, labelled  $I$  (upper zone with degraded mechanical properties) and  $II$  (zone in which the mechanical properties are intact) connected at  $y = 0$ , which is done using stress continuity. The case of the specimen with a crack is different because a frictional stress is present at the debonded interface. Therefore, three zones are required, as shown in Fig. 3.

For validation purposes, material properties defined in Table I were used. The choice of materials was dictated by experimental work [31–34]. Although the theory is developed for orthotropic materials, the validation examples use isotropic materials, which is the most common application of lap-joints. Two adhesives are introduced, one having a brittle tensile behavior, the TGMDA-based epoxy, and one which can yield, the DGEBA-based epoxy, also denoted as a model epoxy network [38]. In these examples, thicknesses of  $2t_1 = t_3 = 4$  mm and  $t_2 = 0.15$  mm were chosen. Typical meshes used in the finite element analyses are shown in Fig. 4. This figure shows a crude mesh. For the calculations in this paper, these elements were refined until convergence was confirmed. For fracture calculations by FEA, the crack surfaces had to be prevented from overlap by using special interface elements.

### 3. Optimal Shear-Lag Analysis

A new shear-lag theory for determining stresses in a multi-layered structure of  $n$  orthotropic layers was recently derived [39]. The multilayered specimen is described by  $n$  layers extending from  $x_{i-1}$  to  $x_i$  for  $i = 1$  to  $n$  with thickness  $t_i = x_i - x_{i-1}$ . The mechanical properties for layer  $i$  include the axial and

Table I. Material properties used in the validations

Material	Modulus (MPa)	Poisson's Ratio	Thermal expansion coefficient (m/m/K)	Shear yield stress (MPa)	Ref.
Aluminum	69000	0.33	2.36E-5	-	[35, 36]
TGMDA epoxy					
- undamaged	3170	0.35	6.7E-5	-	[36]
- damaged	317	0.35	6.7E-5	-	
DGEBA epoxy	1850	0.33	6.67E-5	20	[38, 27]

transverse tensile moduli ( $E_y^{(i)}$  and  $E_x^{(i)}$ ), the shear modulus ( $G_{xy}^{(i)}$ ), the Poisson's ratio ( $\nu_{xy}^{(i)}$ ), and the axial and transverse thermal expansion coefficients ( $\alpha_y^{(i)}$  and  $\alpha_x^{(i)}$ ). Thus, this analysis is for orthotropic materials while a previous simplified analysis, involving isotropic materials only, appeared elsewhere [35, 40]. From an analysis of the most common assumptions used in shear-lag models, it was proposed that the shear stress  $\tau_{xy}^{(i)}(x, y)$  in layer  $i$  can be written as a function of two unknown functions of  $x$  only,  $L_i(x)$  and  $R_i(x)$  (the "left" and "right" shape functions) and the interfacial shear stress  $\tau_{xy}(x_i)$  between layers  $i - 1$  and  $i$  (which are a function only of  $y$ ) as:

$$\tau_{xy}^{(i)}(x, y) = \tau_{xy}(x_{i-1})L_i(x) + \tau_{xy}(x_i)R_i(x) \quad (1)$$

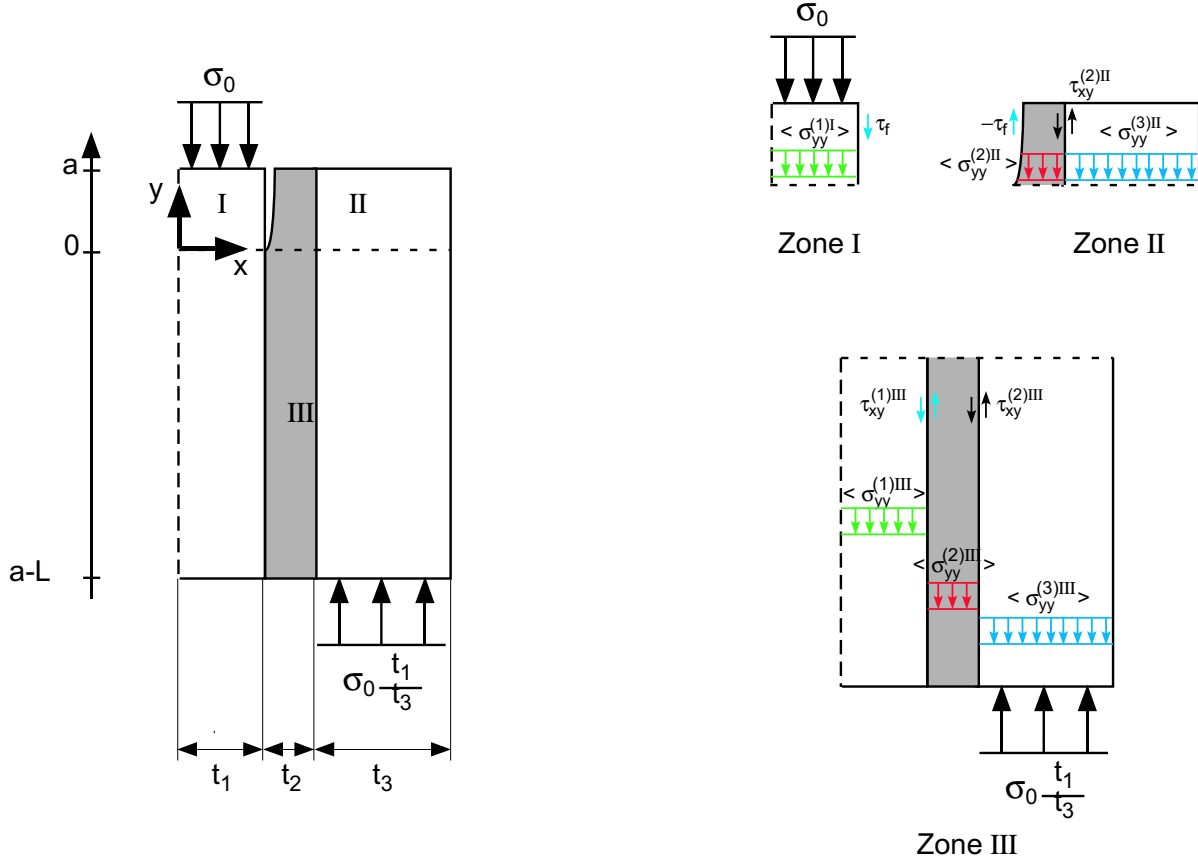


Fig. 3. Geometry of the MDLS specimen with a crack and definition of the three zones ( $I$ ,  $II$ , and  $III$ ) used in the analysis.

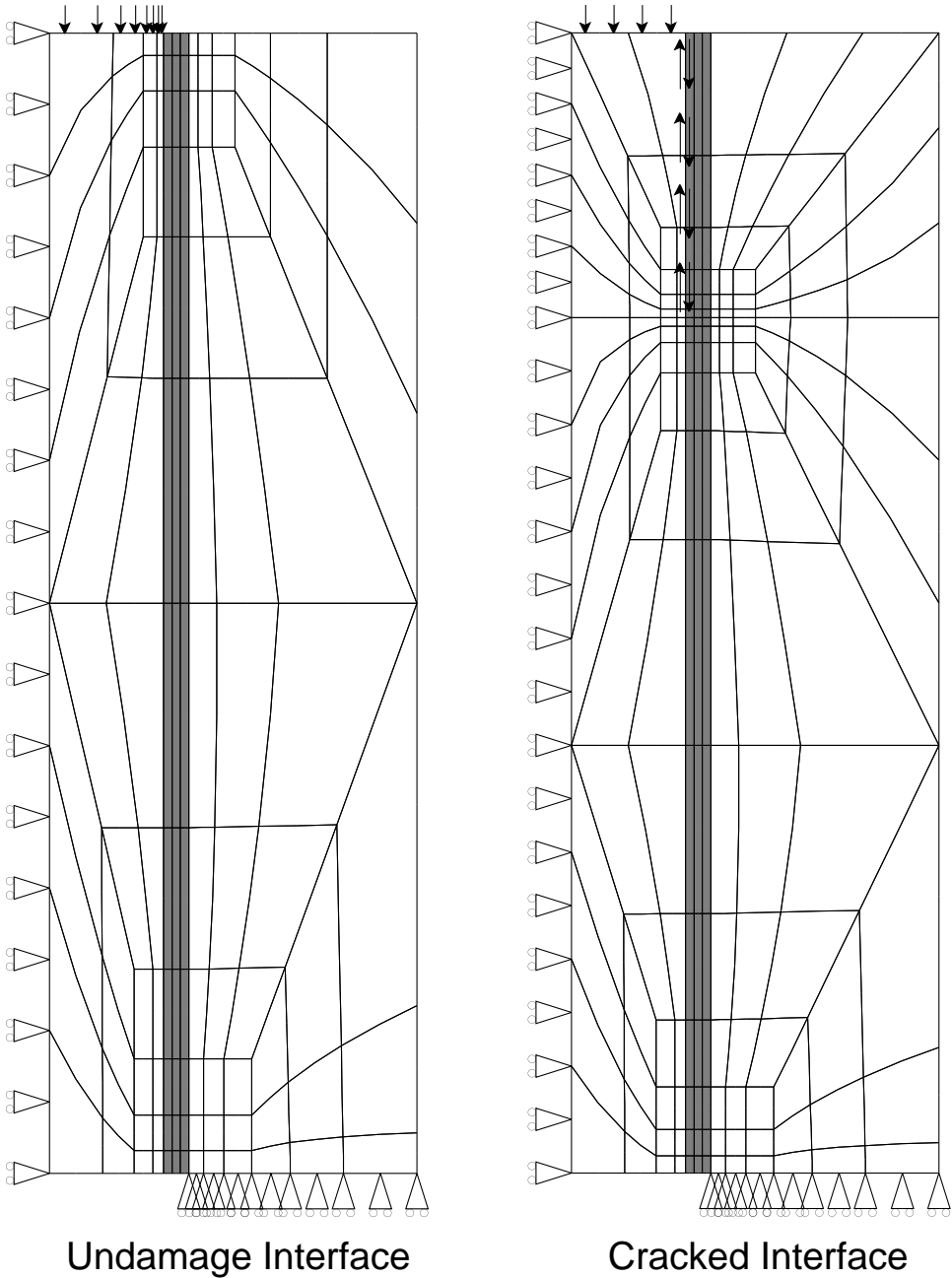


Fig. 4. Meshes used in the finite element analysis for specimens with an undamaged interface or ones with an interfacial crack. For clarity, the adhesive layer is shown thicker than in the actual specimens and not all elements are shown. The converged FEA calculations subdivided each of these elements about three times.

with

$$L_i(x) = \begin{cases} 1 & \text{at } x = x_{i-1} \\ 0 & \text{at } x = x_i \end{cases} \quad (2a)$$

$$R_i(x) = \begin{cases} 0 & \text{at } x = x_{i-1} \\ 1 & \text{at } x = x_i \end{cases} \quad (2b)$$

Defining  $\tau = (\tau_{xy}(x_1), \tau_{xy}(x_2), \dots, \tau_{xy}(x_{n-1}))$ , the shear-lag analysis can be reduced to a system of  $(n-1)$  differential equations in terms of the  $(n-1)$  unknown interfacial shear stresses [39]:

$$[\mathbf{A}] \frac{\partial^2 \tau}{\partial y^2} - [\mathbf{B}] \tau = -\tau_0 \quad (3)$$

where  $[\mathbf{A}]$  and  $[\mathbf{B}]$  are both tridiagonal matrices with elements:

$$\begin{aligned} \mathbf{A}_{i,i-1} &= \frac{t_i \langle \xi_i L_i \rangle}{G_{xy}^{(i)}}, \quad \mathbf{A}_{i,i} = \frac{t_{i+1} \langle (1 - \xi_{i+1}) L_{i+1} \rangle}{G_{xy}^{(i+1)}} + \frac{t_i \langle \xi_i R_i \rangle}{G_{xy}^{(i)}}, \quad \mathbf{A}_{i,i+1} = \frac{t_{i+1} \langle (1 - \xi_{i+1}) R_{i+1} \rangle}{G_{xy}^{(i+1)}} \\ \mathbf{B}_{i,i-1} &= -\frac{1}{E_y^{(i)} t_i}, \quad \mathbf{B}_{i,i} = \frac{1}{E_y^{(i+1)} t_{i+1}} + \frac{1}{E_y^{(i)} t_i}, \quad \mathbf{B}_{i,i+1} = -\frac{1}{E_y^{(i+1)} t_{i+1}} \end{aligned} \quad (4)$$

Here, the dimensionless coordinate in layer  $i$  is defined by

$$\xi_i = \frac{x - x_{i-1}}{t_i} \quad (5)$$

The right side of the equation is defined by:

$$\tau_0 = \left( \frac{\tau_0}{E_y^{(1)} t_1}, 0, \dots, \frac{\tau_n}{E_y^{(n)} t_n} \right) \quad (6)$$

where  $\tau_0$  and  $\tau_n$  are the shear stresses in the middle of the specimen and on the free surface. For all calculations in this paper, except one, these shear stress boundary conditions are zero.

For solution purposes, Eq. (3) is rewritten as:

$$\frac{\partial^2 \tau}{\partial y^2} - [\mathbf{M}_\tau] \tau = -[\mathbf{M}_\tau] [\mathbf{B}]^{-1} \tau_0 \quad (7)$$

where  $[\mathbf{M}_\tau] = [\mathbf{A}]^{-1} [\mathbf{B}]$ . The solution of Eq. (7) is found by an eigen-analysis [39]:

$$\tau_{xy}(x_i) = \tau_0 + \sum_{j=1}^i \frac{t_j E_y^{(j)}}{t E_y^{(0)}} (\tau_n - \tau_0) + \sum_{j=1}^{n-1} (a_j e^{\lambda_j y} - b_j e^{-\lambda_j y}) \omega_{j,i} \quad (8)$$

where  $t = \sum_{i=1}^n t_i$  is the semi-thickness of the composite,  $E_y^{(0)} = \frac{1}{t} \sum_{i=1}^n t_i E_y^{(i)}$  is the rule-of-mixtures effective composite modulus of an undamaged structure in the  $y$  direction,  $\lambda_j^2$  for  $j = 1$  to  $n-1$  are the eigenvalues of the  $[\mathbf{M}_\tau]$  matrix,  $\omega_{j,i}$  is the  $i^{\text{th}}$  element of the eigenvector of  $[\mathbf{M}_\tau]$  associated with  $\lambda_j^2$ , and  $a_j$  and  $b_j$  for  $j = 1$  to  $n-1$  are constants to be determined by boundary conditions. Note that internal stresses do not appear explicitly in this equation, but are included through  $a_j$  and  $b_j$ , calculated as shown below. Additionally, by making use of the equation of equilibrium, it was shown that the average axial stresses are obtained from:

$$\langle \sigma_{yy}^{(i)} \rangle = E_y^{(i)} \left[ \frac{(\tau_0 - \tau_n) + t \sigma_0(0)}{t E_y^{(0)}} + (\alpha_y^{(0)} - \alpha_y^{(i)}) \Delta T \right] + \sum_{j=1}^{n-1} (a_j e^{\lambda_j y} + b_j e^{-\lambda_j y}) \frac{\omega_{j,i-1} - \omega_{j,i}}{t_i \lambda_j} \quad (9)$$

where  $\alpha_y^{(0)}$  is the rule-of-mixtures, effective  $y$ -direction thermal expansion coefficient of an undamaged structure given by:

$$\alpha_y^{(0)} = \sum_{i=1}^n \frac{\alpha_y^{(i)} t_i E_y^{(i)}}{t E_y^{(0)}} \quad (10)$$

Note that  $\sigma_0(y) = (\tau_0 - \tau_n)y + \sigma_0(0)$  is the total applied axial stress in the  $y$ -direction for problems with constant, non-zero shear stresses applied to the sides of the specimen. When there are no shear-stress boundary conditions,  $\sigma_0(y)$  is constant and equal to the total applied axial stress.

The average displacements in the  $y$ -direction in each layer  $i$  can be obtained as a function of the axial displacement at the interface  $x_i$  or at  $x_{i+1}$ , using [39]:

$$\langle v_i \rangle = v(x_i) - \frac{t_i \tau_{xy}(x_{i-1})}{G_{xy}^{(i)}} \langle \xi_i L_i \rangle - \frac{t_i \tau_{xy}(x_i)}{G_{xy}^{(i)}} \langle \xi_i R_i \rangle \quad (11)$$

The average displacement difference across layer  $i$  is thus [39]:

$$\begin{aligned} \langle v_{i+1} \rangle - \langle v_i \rangle &= \frac{t_{i+1} \langle (1 - \xi_{i+1}) R_{i+1} \rangle}{G_{xy}^{(i+1)}} \tau_{xy}(x_{i+1}) + \frac{t_i \langle \xi_i L_i \rangle}{G_{xy}^{(i)}} \tau_{xy}(x_{i-1}) \\ &+ \left( \frac{t_{i+1} \langle (1 - \xi_{i+1}) L_{i+1} \rangle}{G_{xy}^{(i+1)}} + \frac{t_i \langle \xi_i R_i \rangle}{G_{xy}^{(i)}} \right) \tau_{xy}(x_i) \end{aligned} \quad (12)$$

In the following sections these equations are applied to several different analyzes of the MDLS specimen.

## 4. Strength Approach

### 4.1. Specimen Failing in the Linear-Elastic Region

#### 4.1.1. Stress Analysis Solution Method

For a specimen failing in the linear-elastic region, we eliminated the crack and used the modified shear-lag theory with  $n = 3$  layers. The interfacial shear ( $\tau_{xy}^{(i)} = \tau_{xy}(x_i)$ ) and average axial stresses ( $\langle \sigma_{yy}^{(i)} \rangle$ ) are given by [39]:

$$\begin{aligned} \tau_{xy}^{(1)} &= (a_1 e^{\lambda_1 y} - b_1 e^{-\lambda_1 y}) \omega_{1,1} + (a_2 e^{\lambda_2 y} - b_2 e^{-\lambda_2 y}) \omega_{2,1} \\ \tau_{xy}^{(2)} &= (a_1 e^{\lambda_1 y} - b_1 e^{-\lambda_1 y}) \omega_{2,1} + (a_2 e^{\lambda_2 y} - b_2 e^{-\lambda_2 y}) \omega_{2,2} \\ \langle \sigma_{yy}^{(1)} \rangle &= C_1 - (a_1 e^{\lambda_1 y} + b_1 e^{-\lambda_1 y}) \frac{\omega_{1,1}}{\lambda_1 t_1} - (a_2 e^{\lambda_2 y} + b_2 e^{-\lambda_2 y}) \frac{\omega_{2,1}}{\lambda_2 t_1} \\ \langle \sigma_{yy}^{(2)} \rangle &= C_2 - (a_1 e^{\lambda_1 y} + b_1 e^{-\lambda_1 y}) \frac{\omega_{1,2} - \omega_{1,1}}{\lambda_1 t_2} - (a_2 e^{\lambda_2 y} + b_2 e^{-\lambda_2 y}) \frac{\omega_{2,2} - \omega_{2,1}}{\lambda_2 t_2} \\ \langle \sigma_{yy}^{(3)} \rangle &= C_3 + (a_1 e^{\lambda_1 y} + b_1 e^{-\lambda_1 y}) \frac{\omega_{1,2}}{\lambda_1 t_3} + (a_2 e^{\lambda_2 y} + b_2 e^{-\lambda_2 y}) \frac{\omega_{2,2}}{\lambda_2 t_3} \end{aligned} \quad (13)$$

where the constants  $C_i$  define the far-field stress state (*i.e.*, the stresses far away from specimen ends and cracks) and are given by:

$$C_i = E_y^{(i)} \left( -\frac{t_1 \sigma_0}{t E_y^{(0)}} + (\alpha_y^{(0)} - \alpha_y^{(i)}) \Delta T \right) \quad (14)$$

Here  $\sigma_y(0) = -\sigma_0$  where  $\sigma_0$  is the positive magnitude of the applied compressive stress. The remaining constants,  $a_j$  and  $b_j$ ,  $j = 1, 2$ , were determined by the boundary conditions on the average axial stress in the inner adherent and the adhesive layer. With the origin of the system at the middle of the specimen, the boundary conditions are:

$$\langle \sigma_{yy}^{(1)} \rangle \Big|_{y=L/2} = -\sigma_0; \quad \langle \sigma_{yy}^{(1)} \rangle \Big|_{y=-L/2} = 0; \quad \langle \sigma_{yy}^{(2)} \rangle \Big|_{y=\pm L/2} = 0 \quad (15)$$

The average axial stress in the layer 3 is given by force balance. Solving for the four unknowns  $a_1, a_2, b_1, b_2$

as functions of  $C_1$  and  $C_2$  gives:

$$\begin{aligned}
a_1 &= \frac{\sigma_0 e_4 \left( \sinh \left( \frac{\lambda_1 L}{2} \right) + \cosh \left( \frac{\lambda_1 L}{2} \right) \right) - 2 (e_2 C_2 - e_4 C_1) \sinh \left( \frac{\lambda_1 L}{2} \right)}{2 (e_1 e_4 - e_2 e_3) \sinh (\lambda_1 L)} \\
b_1 &= \frac{\sigma_0 e_4 \left( \sinh \left( \frac{\lambda_1 L}{2} \right) - \cosh \left( \frac{\lambda_1 L}{2} \right) \right) - 2 (e_2 C_2 - e_4 C_1) \sinh \left( \frac{\lambda_1 L}{2} \right)}{2 (e_1 e_4 - e_2 e_3) \sinh (\lambda_1 L)} \\
a_2 &= \frac{\sigma_0 e_3 \left( \sinh \left( \frac{\lambda_2 L}{2} \right) + \cosh \left( \frac{\lambda_2 L}{2} \right) \right) - 2 (e_1 C_2 - e_3 C_1) \sinh \left( \frac{\lambda_2 L}{2} \right)}{2 (e_2 e_3 - e_1 e_4) \sinh (\lambda_2 L)} \\
b_2 &= \frac{\sigma_0 e_3 \left( \sinh \left( \frac{\lambda_2 L}{2} \right) - \cosh \left( \frac{\lambda_2 L}{2} \right) \right) - 2 (e_1 C_2 - e_3 C_1) \sinh \left( \frac{\lambda_2 L}{2} \right)}{2 (e_2 e_3 - e_1 e_4) \sinh (\lambda_2 L)}
\end{aligned} \tag{16}$$

where

$$e_1 = \frac{\omega_{1,1}}{\lambda_1 t_1}; \quad e_2 = \frac{\omega_{2,1}}{\lambda_2 t_1}; \quad e_3 = \frac{\omega_{1,2} - \omega_{1,1}}{\lambda_1 t_2}; \quad e_4 = \frac{\omega_{2,2} - \omega_{2,1}}{\lambda_2 t_2} \tag{17}$$

The obtained set of equations presents a full, closed form solution of both axial and shear stresses in the MDLS sample. This solution depends upon the choice of shape functions which enter in the definition of matrix  $[\mathbf{A}]$ . For a three-layer problem, the final solution depends only on six dimensionless averages of the shape function in the layers, namely  $\langle \zeta_1 R_1 \rangle$ ,  $\langle (1 - \zeta_2) L_2 \rangle$ ,  $\langle (1 - \zeta_2) R_2 \rangle$ ,  $\langle \zeta_2 L_2 \rangle$ ,  $\langle \zeta_2 R_2 \rangle$  and  $\langle (1 - \zeta_3) L_3 \rangle$ .

#### 4.1.2. The Influence of Shape Functions

The solution in the previous section was compared to FEA results for various shape functions. A common assumption in prior shear-lag methods is to take all shape function as linear, which implies  $L_i = 1 - \xi_i$  and  $R_i = \xi_i$ . The required averages reduce to

$$\langle \xi_i L_i \rangle = \frac{1}{6}; \quad \langle (1 - \xi_i) L_i \rangle = \frac{1}{3}; \quad \langle \xi_i R_i \rangle = \frac{1}{3}; \quad \langle (1 - \xi_i) R_i \rangle = \frac{1}{6} \tag{18}$$

The plot shown in Fig. 5 shows reasonable agreement with FEA results, particularly in terms of stress integral, corresponding to the elastic energy stored in the system (*c.f.* Ref. [39]). Like all shear-lag models, this analysis fails to give zero shear stress on the ends because of a lack of degrees of freedom in the shear-lag analysis. The solution makes use of all axial stress boundary conditions to find the unknown constants and can not therefore satisfy additional boundary conditions such as zero shear stress on the end. Instead, the shear stress reaches a maximum value on the ends. The FEA results show peaks very near the ends and then tend towards zero, although never become exactly zero. The FEA results show that there are indeed shear stress maxima very close to the ends of the specimen. More accurate analytical or numerical results would require accounting for the singularity existing at the interface between two different media at a boundary. This problem, however, remains unsolved for such complex geometry, and approximate solutions are needed. The maximum shear stress at the end of the shear-lag solution can be regarded as an approximate representation of the real shear stress peak and therefore an approximate accounting for the singularity effects.

It is possible to refine the shear-lag solution by selecting non-linear shape functions; the approach is similar to that used for a single fibre or a platelet embedded in an infinite elastic medium [37]. Because the adhesive layer is very thin, it is likely that linear shape functions are sufficient. Even if the adhesive layer shear stress is non-linear, the effect on the final solution is expected to be negligible. Thus  $L_2$  and  $R_2$  are assumed to be linear as in the previous calculations. The remaining shape function averages,  $\langle \zeta_1 R_1 \rangle$  and  $\langle (1 - \zeta_3) L_3 \rangle$ , were then regarded as unknowns; the best values were found by fitting FEA results. The best agreement with FEA for the average axial stresses  $\langle \sigma_{yy}^{(1)} \rangle$  and  $\langle \sigma_{yy}^{(3)} \rangle$  was obtained when the two eigenvectors were orthonormal. Such eigenvectors are  $(1/\sqrt{2} \ 1/\sqrt{2})$  and  $(-1/\sqrt{2} \ 1/\sqrt{2})$ . Next  $\langle \xi_1 R_1 \rangle$  and  $\langle (1 - \xi_3) L_3 \rangle$  were obtained by an inverse method to that used to obtain these eigenvectors. Since the process also changes the eigenvalues, one repeats all the calculation steps. Interestingly, the best fitting values were found to be close to:

$$\langle \xi_1 R_1 \rangle = \frac{E_y^{(1)} t_1}{E_y^{(0)} t}; \quad \langle (1 - \xi_3) L_3 \rangle = \frac{E_y^{(3)} t_3}{E_y^{(0)} t} \tag{19}$$

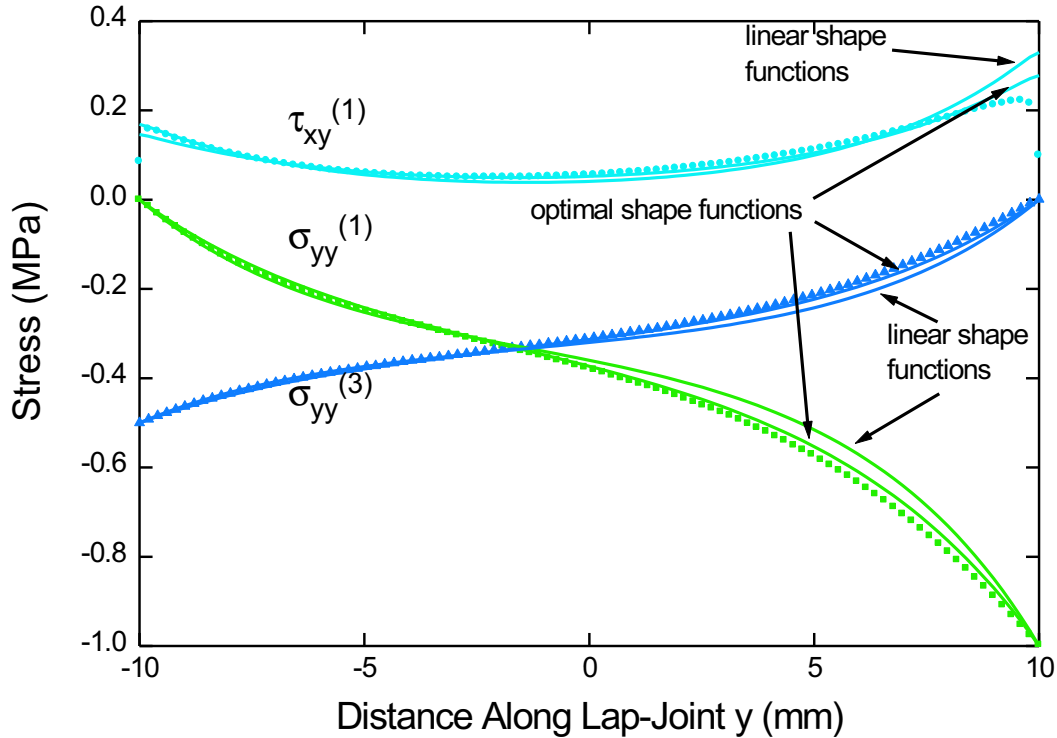


Fig. 5. Axial and shear stresses *vs.* distance along lap-joint, linear and optimal shape function solutions (TGMDA-based epoxy adhesive, stresses are normalized vs.  $\sigma_0$ , and  $\Delta T = 0$ )

In other words, the optimal shape function averages were equal to the fraction of the specimen stiffness contributed by that layer.

Figure 5 plots the stresses obtained using optimal shape function, in comparison to those obtained with linear shape functions. The solution is improved by the use of refined shape functions. The average axial stresses in the adherents are nearly exact to the FEA results. The shear stress calculation is improved but still has the limitation of all shear-lag models of maximum shear stress on the ends instead of zero shear stress. It should be noted that FEA results do not provide an exact solution either, since this method does not deal with interfaces in a continuous way, *i.e.*, stresses and their derivatives are non continuous across the interface. Therefore, the optimal shear-lag method presented here, representing the best shear-lag solution, together with the use of its shape functions, is believed to be accurate on the level of FEA results to serve as a basis for further investigations.

The plots show average axial stresses and shear stresses. Shear lag can also find average axial displacements and they similarly agree with FEA results. Shear lag has used to find other terms, such as transverse stresses or displacements, but such results are not accurate [39]. In fracture mechanics calculations, it is necessary to find total strain energy in the specimen. Because the strain energy in the MDLS specimen can be found using boundary integrals and reduced to a result that depends only on axial stresses and displacements, this energy can be found accurately by shear-lag analysis [39].

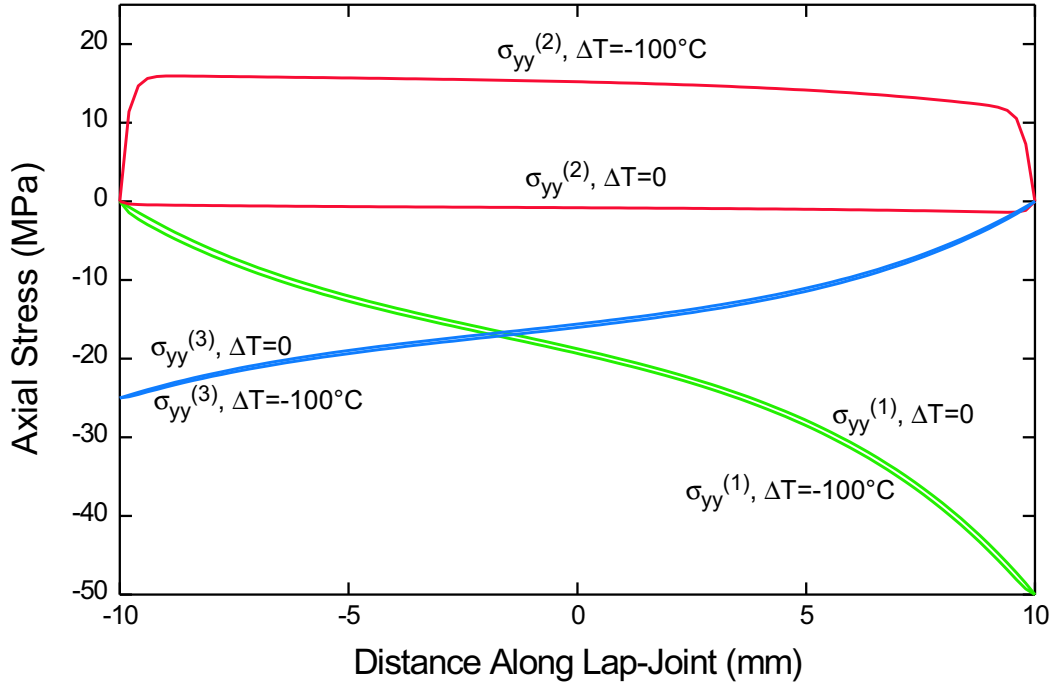


Fig. 6. Axial stresses *vs.* distance along a lap-joint, TGMDA-based epoxy adhesive, solution with hyperbolic shape functions, including internal stresses as indicated on the figure by  $\Delta T$ ,  $\sigma_0 = 50$  MPa.

#### 4.1.3. Influence of Internal Stresses

Internal stresses are included and enter the solution through the constants  $C_i$ . Previous calculation used  $\Delta T = 0$ ; some more results for axial and shear stresses when  $\Delta T \neq 0$  are given in Figs. 6 and 7, respectively. Figure 6 compares the contributions of internal stresses to the axial stresses in the system. It is obvious that the stress state in the adhesive layer is greatly affected. The residual stresses have only a small effect, however, on the axial stresses of the adherents, which agrees with experimental measurements [24]. Most of the experimental work found in the literature was derived by measuring the displacements in the adherents using either strain gages or interferometric methods. The minor influence of the adhesive internal stress state on the adherents axial stress probably explains why internal stresses have been neglected in the corresponding analysis of the test. This approach has led to crude approximations, since internal stresses are shown to generate high axial stress and shear stresses in the adhesive layer.

As seen in Fig. 7, the shear stress at the adhesive-outer adherent interface,  $\tau_{xy}^{(2)}$ , is substantially increased upon the introduction of internal stresses, while the shear stress at the adhesive-inner adherent interface,  $\tau_{xy}^{(1)}$ , is decreased down to a negative value. This formalism can be used to describe the onset of crack propagation at the interface of a double lap shear specimen [32, 35]. It was found interesting to compare several cure conditions or model systems with additives, by which the internal stress level could be varied. To analyze these tests, it is important to isolate the residual stress terms. Defining  $K_i, i = 1, 2$ , as the thermal stress terms in the constants  $C_1$  and  $C_2$  by writing:

$$K_i = E_y^{(i)} \left( \alpha_y^{(0)} - \alpha_y^{(i)} \right) \Delta T \quad (20)$$

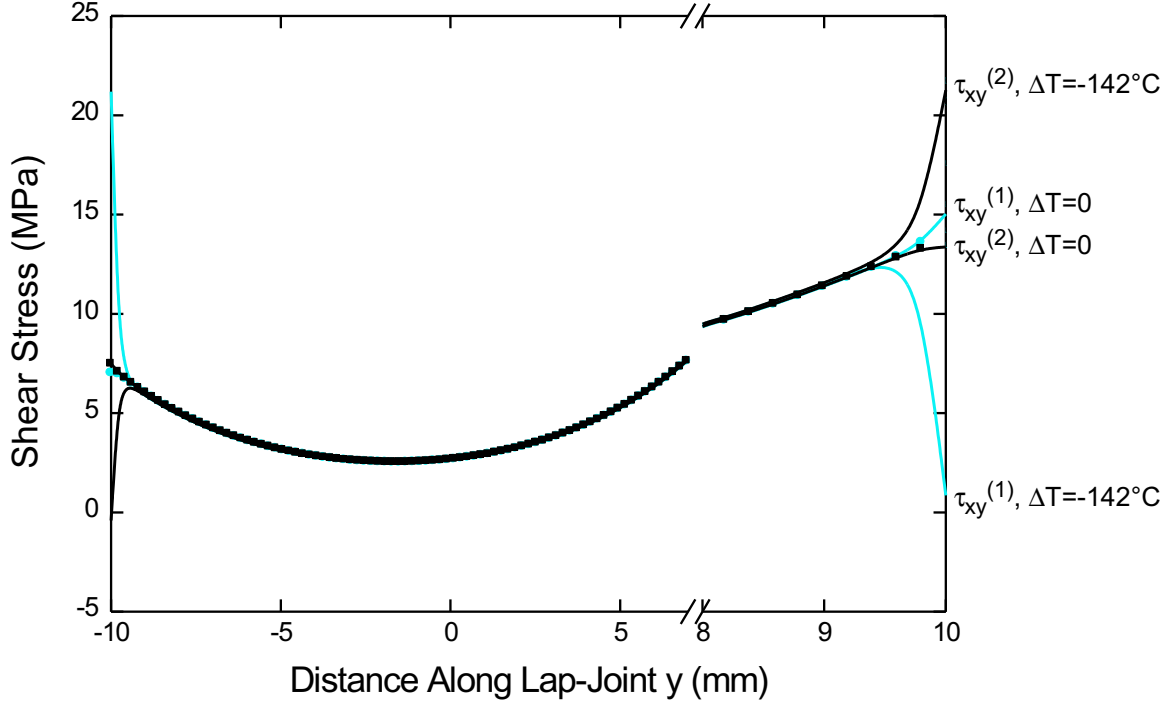


Fig. 7. Shear stresses *vs.* distance along a lap-joint, TGMDA-based epoxy adhesive, solution with hyperbolic shape functions, including internal stresses as indicated on the figure by  $\Delta T$ ,  $\sigma_0 = 50$  MPa.

The shear stress on the inner surface of the adhesive at  $y = L/2$  can be written as:

$$\tau_{xy}^{(1)} \Big|_{y=L/2} = \sigma_0 \zeta_1 + \chi_1 \quad (21)$$

where

$$\zeta_1 = \omega_{1,1} \frac{e_4 \cosh(\lambda_1 L) t E_y^{(0)} + 2t_1 (e_2 E_y^{(2)} - e_4 E_y^{(1)}) \sinh^2(\frac{\lambda_1 L}{2})}{(e_1 e_4 - e_2 e_3) \sinh(\lambda_1 L) t E_y^{(0)}} - \omega_{2,1} \frac{e_3 \cosh(\lambda_2 L) t E_y^{(0)} + 2t_1 (e_1 E_y^{(2)} - e_3 E_y^{(1)}) \sinh^2(\frac{\lambda_2 L}{2})}{(e_1 e_4 - e_2 e_3) \sinh(\lambda_2 L) t E_y^{(0)}} \quad (22)$$

and

$$\chi_1 = -\omega_{1,1} \frac{e_2 K_2 - e_4 K_1}{e_1 e_4 - e_2 e_3} \tanh\left(\frac{\lambda_1 L}{2}\right) + \omega_{2,1} \frac{e_1 K_2 - e_3 K_1}{e_1 e_4 - e_2 e_3} \tanh\left(\frac{\lambda_2 L}{2}\right) \quad (23)$$

The shear stress on the other surface of the adhesive is given by:

$$\tau_{xy}^{(2)} \Big|_{y=L/2} = \sigma_0 \zeta_2 + \chi_2 \quad (24)$$

where

$$\begin{aligned} \zeta_2 = \omega_{1,2} & \frac{e_4 \cosh(\lambda_1 L) tE_y^{(0)} + 2t_1 (e_2 E_y^{(2)} - e_4 E_y^{(1)}) \sinh^2\left(\frac{\lambda_1 L}{2}\right)}{(e_1 e_4 - e_2 e_3) \sinh(\lambda_1 L) tE_y^{(0)}} \\ & - \omega_{2,2} \frac{e_3 \cosh(\lambda_2 L) tE_y^{(0)} + 2t_1 (e_1 E_y^{(2)} - e_3 E_y^{(1)}) \sinh^2\left(\frac{\lambda_2 L}{2}\right)}{(e_1 e_4 - e_2 e_3) \sinh(\lambda_2 L) tE_y^{(0)}} \end{aligned} \quad (25)$$

and

$$\chi_2 = -\omega_{1,2} \frac{e_2 K_2 - e_4 K_1}{e_1 e_4 - e_2 e_3} \tanh\left(\frac{\lambda_1 L}{2}\right) + \omega_{2,2} \frac{e_1 K_2 - e_3 K_1}{e_1 e_4 - e_2 e_3} \tanh\left(\frac{\lambda_2 L}{2}\right) \quad (26)$$

This formulation is useful because it splits the apparent interfacial shear strength for applied mechanical loads into internal stress effects and the true shear stresses required for debonding. Writing the experimental shear stress at failure in terms of the applied compression stress as

$$\tau_{exp} = \frac{F}{2WL} = \sigma_0 \frac{t_1}{L} \quad (27)$$

one obtains at failure:

$$\tau_{xy}^{(1)} \Big|_{y=L/2} = \tau_0 = \tau_{exp} \frac{L}{t_1} \zeta_1 + \chi_1 \quad (28)$$

$$\Rightarrow \tau_{exp} = \frac{t_1}{L \zeta_1} (\tau_0 - \chi_1) \quad (29)$$

or, if debonding starts on the other interface:

$$\tau_{exp} = \frac{t_1}{L \zeta_2} (\tau_0 - \chi_2) \quad (30)$$

In this formalism,  $\tau_0$  represents the true, local shear strength of the interface, which does not depend on internal stresses or on the geometry. In contrast, the observed experimental shear strength,  $\tau_{exp}$ , is affected both by interfacial properties and by residual stresses effects. In brief,  $\tau_0$  is the more fundamental property for characterization of the interface. This simplified analysis was found to be robust enough to analyze experimental data for the onset of debonding, when the specimen failed in the linear-elastic regime.

#### 4.2. Stresses in a Transversely Cracked Specimen

The problem of stresses when the adhesive is damaged by transverse cracks arises from experimental observations in Ref. [32]. It was observed that some brittle epoxy adhesives transversely crack prior to debonding. The extent of transverse cracking was reproducible. This section establishes the equations necessary for describing this phenomenon. Consider a damaged zone of length  $d$  as shown in Fig. 2. As a first approximation, we considered that the shear modulus of the adhesive, and thereby its Young's modulus too, were reduced by transverse cracking. This hypothesis was well supported by the stress-strain curves obtained during loading of the MDLS specimen, which showed a decrease of the effective modulus of the joint. Using this hypothesis, the stresses of the system could be found by analyzing two zones with distinct mechanical properties for the adhesive, and making axial and shear stresses continuous across the two zones. The stress in the two zones are each given by Eq. (13) except that separate constants are needed for each zone or  $a_j \rightarrow a_j^k$ ,  $b_j \rightarrow b_j^k$ ,  $C_j \rightarrow C_j^k$ ,  $\omega_{j,i} \rightarrow \omega_{j,i}^k$ , and  $\lambda_j \rightarrow \lambda_j^k$  where  $k = I, II$ . The constants  $C_j^k$  are given by Eq. (14) using  $E_y^{(i)k}$  and  $\alpha_y^{(i)k}$  for layer properties and rule-of-mixtures results redefined as

$$E_y^{(0)k} = \frac{E_y^{(1)} t_1 + E_y^{(2)k} t_2 + E_y^{(3)} t_3}{t} \quad (31)$$

$$\alpha_y^{(0)k} = \frac{\alpha_y^{(1)} E_y^{(1)} t_1 + \alpha_y^{(2)} E_y^{(2)k} t_2 + \alpha_y^{(3)} E_y^{(3)} t_3}{t E_y^{(0)k}} \quad (32)$$

Notice that only the mechanical properties of layer 2 differ between zones I and II. The eight unknown constants,  $a_j^k$ ,  $b_j^k$  with  $j = 1, 2$  were obtained from the following the eight boundary conditions:

$$\begin{aligned} \langle \sigma_{yy}^{(2)I} \rangle \Big|_{y=d} &= 0; & \langle \sigma_{yy}^{(2)II} \rangle \Big|_{y=d-L} &= 0; & \langle \sigma_{yy}^{(1)I} \rangle \Big|_{y=d} &= -\sigma_0 \\ \langle \sigma_{yy}^{(1)II} \rangle \Big|_{y=d-L} &= 0; & \langle \sigma_{yy}^{(2)I} \rangle \Big|_{y=0} &= \langle \sigma_{yy}^{(2)II} \rangle \Big|_{y=0}; & \langle \sigma_{yy}^{(1)I} \rangle \Big|_{y=0} &= \langle \sigma_{yy}^{(1)II} \rangle \Big|_{y=0} \\ \tau_{xy}^{(1)I} \Big|_{y=0} &= \tau_{xy}^{(1)II} \Big|_{y=0}; & \tau_{xy}^{(2)I} \Big|_{y=0} &= \tau_{xy}^{(2)II} \Big|_{y=0} \end{aligned} \quad (33)$$

Figure 8 shows the distribution of stresses in the adhesive joint submitted to internal stresses and applied stress, considering a fragmented zone of length  $d = 3$  mm in which  $E_y^{(i)I} = 0.1E_y^{(1)II}$  or damage caused 90% degradation. This value was set arbitrarily, based on those obtained from fitting the force vs. displacement curves of TGMDA-based specimens used in experiments detailed elsewhere [32]. It will be further shown that the experimental stress-strain curve is modelled accurately by the present theory, the major difficulty being the determination of the onset of transverse microcracking. On this plot the two zones connected at the origin  $y = 0$  clearly appear, and they involve a local reduction of the axial tensile stress in the damaged adhesive which is essentially due to Young's modulus reduction and the release of internal stresses it induces. The shear stress profiles are still influenced by internal stresses, which involve a stress increase at the loaded end of the specimen ( $y = 3$  on Fig. 8).

More information than available would be needed to accurately calculate the modulus reduction in the fragmented zone: the angle of the transverse crack with the interface plane is usually observed to be close to  $45^\circ$ , but some variations were observed between specimens with different internal stress states; the distance between two consecutive fragments would also provide useful information on the rate of the damage propagation. As a consequence, the present analysis, which uses an average loss of mechanical properties, is a first approximation of the fracture mechanics involved in the process. Accurate modelling of the local stress state and fracture mechanics involving fragmentation nucleation, propagation, as well as the friction between fragments, would better describe the residual properties of the fragmented adhesive zone. Nevertheless, one of the attractive features of this model is to quantify the fracture process efficiently by describing initiation, propagation and first adhesive failure of the joint, as will be illustrated by experimental results in Ref. [32].

#### 4.3. Specimen with a Partially Yielded Adhesive

For this analysis, the adhesive was considered as a time-independent, elastic-perfectly-plastic material. Viscoelastic relaxation of internal stresses can be included by using an effective temperature step, as described in Ref. [33]. One can then model the MDLS specimen as two connected zones with different properties (Fig. 2): a first zone in which the adhesive yields and which is characterized by a constant shear stress, connected to a second zone in which the adhesive has an elastic behavior. This case resembles the previous one, in which zone *I* had altered properties. One major difference arises: for a yielded interface, the yield stress can be evaluated experimentally while it is more difficult to determine the correct results to use for a degraded modulus.

In this analysis, the shear stress in zone *I* is a constant  $\tau_p$  equal to the shear yield stress of the adhesive, which leads to zone *I* stress state of:

$$\tau_{xy}^{(1)I} = \tau_{xy}^{(2)I} = \tau_p; \quad \langle \sigma_{yy}^{(1)I} \rangle = \frac{\tau_p}{t_1} (d - y) - \sigma_0; \quad \langle \sigma_{yy}^{(3)I} \rangle = \frac{\tau_p}{t_3} (y - d) \quad (34)$$

Because the shear stress in layer 2 is constant (and also by force balance), the average stress in the adhesive in zone *I* ( $\langle \sigma_{yy}^{(2)I} \rangle$ ) is zero. The zone *II* stress state is again given by Eq. (13). The boundary conditions for the four unknowns in zone *II* involve the continuity of axial stresses between the two zones, and the free end conditions:

$$\begin{aligned} \langle \sigma_{yy}^{(1)I} \rangle \Big|_{y=0} &= \langle \sigma_{yy}^{(1)II} \rangle \Big|_{y=0}; & \langle \sigma_{yy}^{(1)II} \rangle \Big|_{y=d-L} &= 0 \\ \langle \sigma_{yy}^{(2)I} \rangle \Big|_{y=0} &= \langle \sigma_{yy}^{(2)II} \rangle \Big|_{y=0} = 0; & \langle \sigma_{yy}^{(2)II} \rangle \Big|_{y=d-L} &= 0 \end{aligned} \quad (35)$$

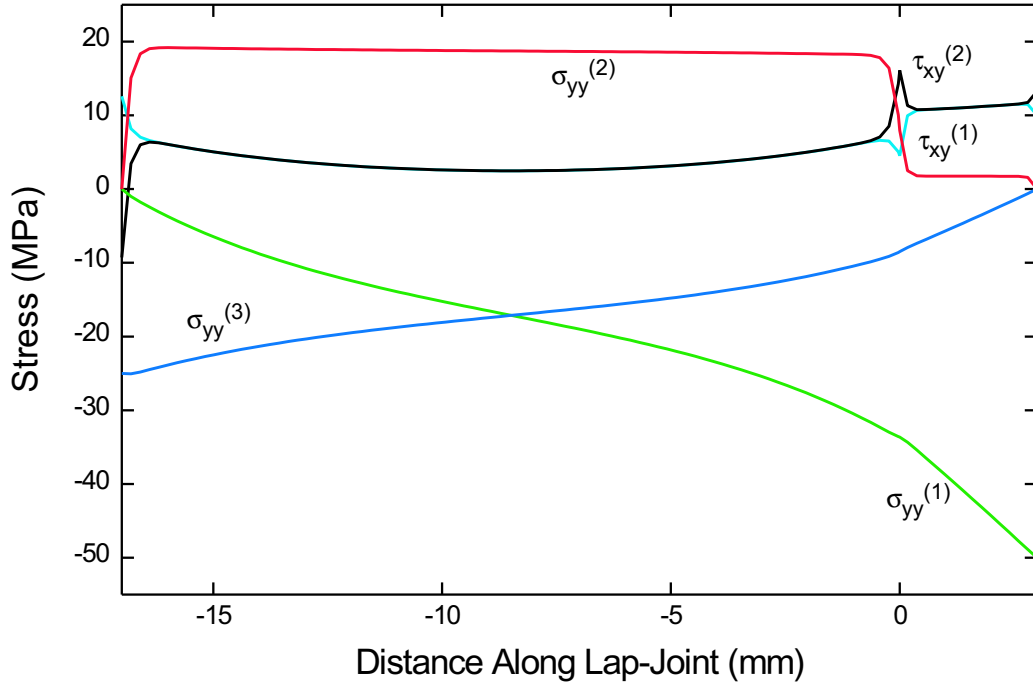


Fig. 8. Stresses *vs.* distance along a lap-joint, with a damage zone of length  $d = 3$  mm, TGMDA-based epoxy adhesive, Young's modulus  $E_2^I = 0.1 \cdot E_2^{II}$ ,  $\Delta T = -100^\circ\text{C}$ , and  $\sigma_0 = -50$  MPa

Sample calculations obtained following this approach are shown in Fig. 9. Interestingly, the interfacial shear stresses  $\tau_{xy}^{(1)}$  and  $\tau_{xy}^{(2)}$  can be superposed almost everywhere, except close to the unloaded end of the specimen at  $y = d - L$ , where they differ by less than one percent. In this model,  $\tau_{xy}^{(1)} = \tau_{xy}^{(2)}$  throughout the yield zone and at the tip of the yield zone. This analysis can thus not predict which interface will debond first. On the other hand, this model is remarkably accurate for describing the interfacial strength of specimens having similar interface characteristics but different shear yield stresses (see Ref. [33]).

#### 4.4. Determination of Stresses in a Cracked Specimen (Three Zone Model)

To interpret experiments in which a crack propagates along the interface, we considered a specimen with a crack of length  $a$  at the interface between layer 1 and 2. The origin of the  $y$  axis is located at the crack tip. The analysis proceeds by considering three zones as indicated in Fig. 3. The stresses in zone III are again given by Eq. (13). The two new zones were analyzed as follows:

##### 4.4.1. Zone I

The stresses in zone I can be obtained by considering the shear stress as zero in the midplane and increasing linearly to a constant shear stress on the crack denoted by  $\tau_f$  (the positive magnitude of the friction stress on the crack). Two singularities of the problem are neglected at  $y = a$  and  $y = 0$ , where the shear stress of the cracked interface should be zero and singular, respectively. At  $y = a$ , it is not necessary to refine the problem by introducing a zone of infinitely small length, as was done for other types of load and geometry

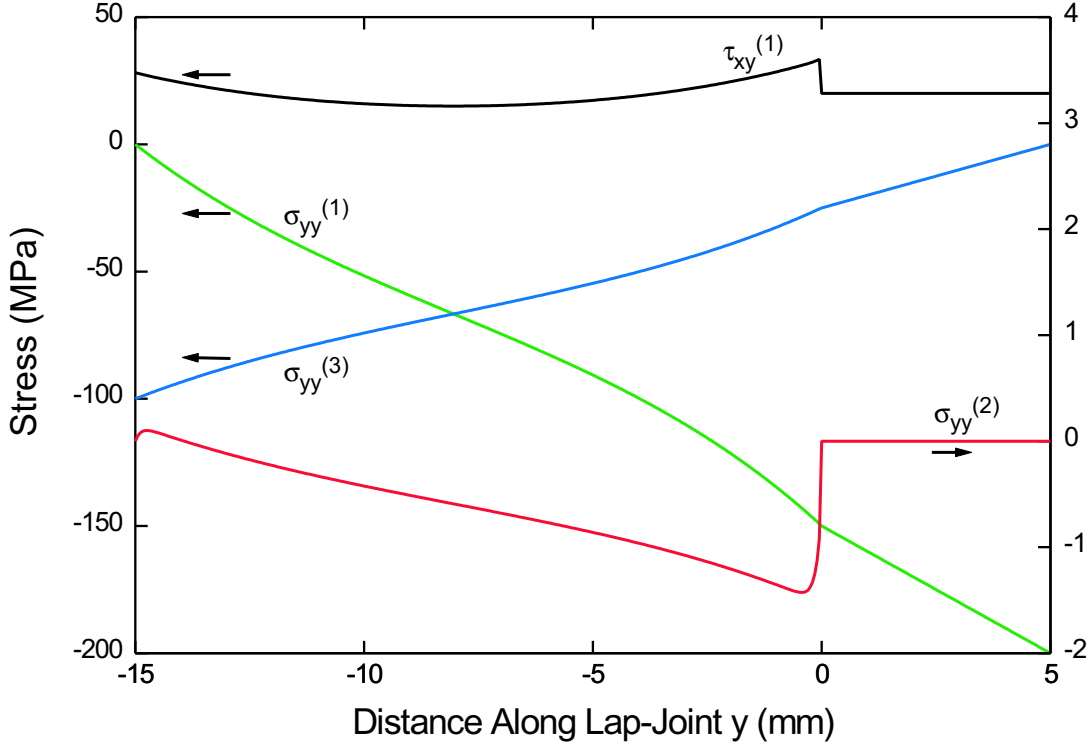


Fig. 9. Stresses *vs.* distance along a lap-joint, DGEBA-based epoxy adhesive, solution with hyperbolic shape functions, including constant shear stress  $\tau_p = 20$  MPa in the yielded zone,  $\sigma_0 = 200$  MPa,  $\Delta T = -15^\circ\text{C}$ .

[41, 42, 43], because the ERR does not depend on the shear stress  $\tau_{xy}(a)$ . The singularity at  $y = 0$  is more of a problem, and the accuracy of the model should be checked at that location.

Force equilibrium on an element of length  $dy$  leads to (see Ref. [39] for details):

$$\frac{\partial \langle \sigma_{yy}^{(1)I} \rangle}{\partial y} = -\frac{\tau_f}{t_1} \quad (36)$$

Using the boundary condition:

$$\langle \sigma_{yy}^{(1)I} \rangle \Big|_{y=a} = -\sigma_0 \quad (37)$$

the zone I axial stress is:

$$\langle \sigma_{yy}^{(1)I} \rangle = \tau_f \frac{a-y}{t_1} - \sigma_0 \quad (38)$$

#### 4.4.2. Zone II

In zone II, the friction stress in the debonded interface is of opposite sign to that of zone I, and therefore equals  $-\tau_f$ . This case corresponds to a two-layer, shear-lag analysis with non-zero boundary shear stress. It can be solved using the following equation [39]:

$$\frac{\partial^2 \tau_{xy}^{(2)II}}{\partial y^2} - \beta^2 \tau_{xy}^{(2)II} = \frac{\tau_f}{E_y^{(2)} t_2} \frac{1}{\frac{t_2}{3G_{xy}^{(2)}} + \frac{t_3}{3G_{xy}^{(3)}}} \quad (39)$$

where the optimal shear-lag parameter is

$$\beta^2 = \frac{\frac{1}{E_y^{(2)} t_2} + \frac{1}{E_y^{(3)} t_3}}{\frac{t_2}{3G_{xy}^{(2)}} + \frac{t_3}{3G_{xy}^{(3)}}} \quad (40)$$

Solving Eq. (39), one obtains:

$$\begin{aligned} t_2 \langle \sigma_{yy}^{(2)II} \rangle &= a^{II} e^{\beta y} + b^{II} e^{-\beta y} + E_y^{(2)} t_2 \left( \frac{\tau_f (y-a)}{E_y^{(0)II} (t_2 + t_3)} + (\alpha_y^{(0)II} - \alpha_y^{(2)}) \Delta T \right) \\ t_3 \langle \sigma_{yy}^{(3)II} \rangle &= -a^{II} e^{\beta y} - b^{II} e^{-\beta y} + E_y^{(3)} t_3 \left( \frac{\tau_f (y-a)}{E_y^{(0)II} (t_2 + t_3)} + (\alpha_y^{(0)II} - \alpha_y^{(3)}) \Delta T \right) \\ \tau_{xy}^{(2)II} &= \frac{E_y^{(3)} t_3 \tau_f}{(t_2 + t_3) E_y^{(0)II}} - \beta a^{II} e^{\beta y} + \beta b^{II} e^{-\beta y} \end{aligned} \quad (41)$$

and  $E_y^{(0)II}$  and  $\alpha_y^{(0)II}$  are the rule-of-mixtures properties for the system with 2 layers, i.e.:

$$\begin{aligned} E_y^{(0)II} &= \frac{E_y^{(2)} t_2 + E_y^{(3)} t_3}{t_2 + t_3} \\ \alpha_y^{(0)II} &= \frac{\alpha_y^{(2)} E_y^{(2)} t_2 + \alpha_y^{(3)} E_y^{(3)} t_3}{E_y^{(0)II} (t_2 + t_3)} \end{aligned} \quad (42)$$

#### 4.4.3. Boundary Conditions

The above stresses have six unknowns:  $a^{II}$ ,  $b^{II}$ ,  $a_1^{III}$ ,  $b_1^{III}$ ,  $a_2^{III}$ , and  $b_2^{III}$ . These unknowns were determined from the following six boundary conditions:

$$\begin{aligned} \langle \sigma_{yy}^{(2)II} \rangle \Big|_{y=a} &= 0; & \langle \sigma_{yy}^{(2)II} \rangle \Big|_{y=0} &= \langle \sigma_{yy}^{(2)III} \rangle \Big|_{y=0}; & \langle \sigma_{yy}^{(1)III} \rangle \Big|_{y=0} &= \tau_f a - t_1 \sigma_0 \\ \langle \sigma_{yy}^{(1)III} \rangle \Big|_{y=a-L} &= 0; & \langle \sigma_{yy}^{(2)III} \rangle \Big|_{y=a-L} &= 0; & \tau_2^{III} \Big|_{y=0} &= \tau_2^{II} \Big|_{y=0} \end{aligned} \quad (43)$$

As shown in Figs. 10 and 11, the stresses found by this analysis agree well with FEA results for a cracked specimen.

## 5. Energy Release Rate

Using the stress state in the previous section, it is possible to calculate the energy release rate for growth of an interfacial crack. The calculation of the energy release rate proceeds in two steps. First, an exact expression for the energy release rate which can be reduced to a result that depends only on axial displacements and average axial stresses is derived. Second, the shear-lag results for these displacements and stresses are used to derive an approximate energy release rate.

### 5.1. Exact Results

A general result for energy release rate in composite fracture which includes residual stresses and traction loads on cracks (*e.g.*, friction) was recently derived as [16]:

$$G = \frac{1}{2} \frac{\partial}{\partial A} \left( \int_{S+S_c} \vec{T}^0 \cdot \vec{u} dS + \int_V \sigma \alpha \Delta T dV \right) \quad (44)$$

where  $A$  is the cracked area,  $S$  denotes the outer surface,  $S_c$  stands for the cracked surfaces, and  $V$  denotes the volume.  $\vec{T}^0$  is the traction loads which are applied to  $S$  and possibly also on  $S_c$ , and  $\vec{u} = (u, v, w)$  where the components are the displacements in the  $x, y$ , and  $z$  directions.

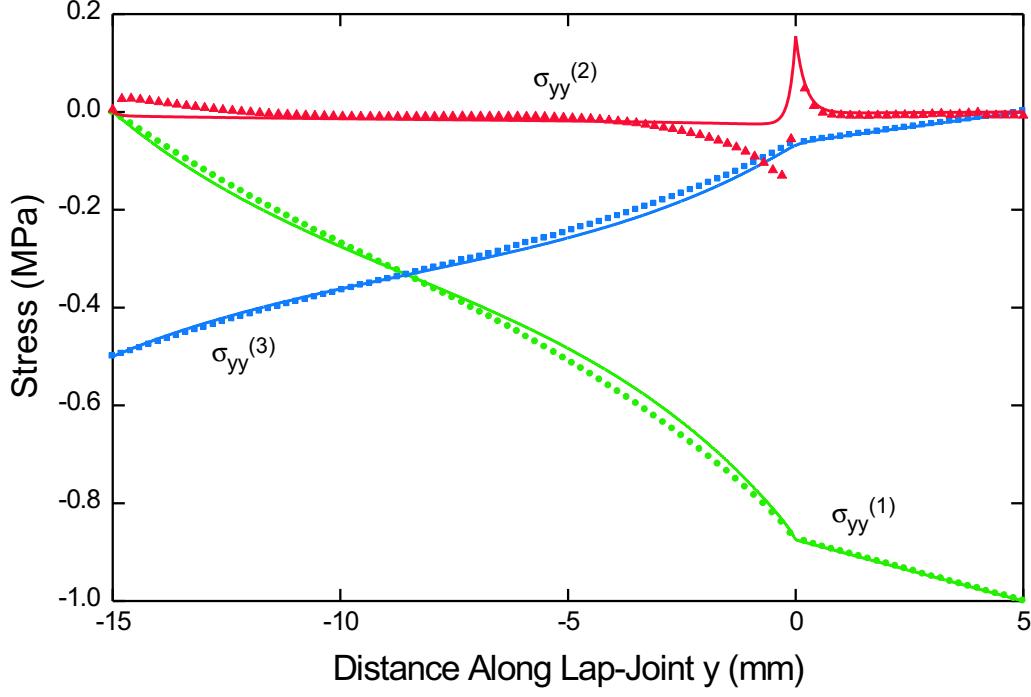


Fig. 10. Normalized axial stresses *vs.* distance along a lap-joint, TGMDA-based epoxy adhesive, solution with hyperbolic shape functions, including constant friction in debond zone ( $\tau_f = 0.05\sigma_0$ ),  $\Delta T = 0$ ).

Table II. Calculation of the traction-displacement integrals for all loaded boundary surfaces and traction-loaded crack surfaces.

Surface	$\vec{T}^0$	$\vec{u}$	$\int_{S+S_c} \vec{T}^0 \cdot \vec{u} dS$
top plate 1	$(0 \ -\sigma_0 \ 0)$	$(u_1 \ v_1(x, a) \ w_1)$	$-\sigma_0 t_1 W \langle v_1(a) \rangle$
bottom plate 3	$(0 \ \sigma_0 \frac{t_1}{t_3} \ 0)$	$(u_3 \ v_3(x, a) \ w_3)$	$\sigma_0 t_1 W \langle v_3(a-L) \rangle$
crack surface, plate 1	$(-\sigma_t \ \tau_f \ 0)$	$(u_1(t_1, y) \ v_1(t_1, y) \ w_1)$	$W \int_0^a \tau_f (v_1(t_1, y) - v_2(t_1, y)) dy$
crack surface, plate 2	$(\sigma_t \ -\tau_f \ 0)$	$(u_2(t_1, y) \ v_2(t_1, y) \ w_2)$	
crack surfaces <sup>†</sup>			
side surface	$(-\sigma_t \ 0 \ 0)$	$(u_3(t, y) \ v_3 \ w_3)$	$-\sigma_t L W \langle u_3(t) \rangle$

<sup>†</sup> From the two preceding lines  $\vec{T}^0 \cdot \vec{u} = -\sigma_t u_1(t_1) + \tau_f v_1(t_1, y) - \tau_f v_2(t_1, y) + \sigma_t u_2(t_1)$ , but the transverse stress terms cancel because either  $u_1(t_1) = u_2(t_1)$ , when the crack surfaces are in contact, or  $\sigma_t = 0$ , when the crack surfaces are not in contact.

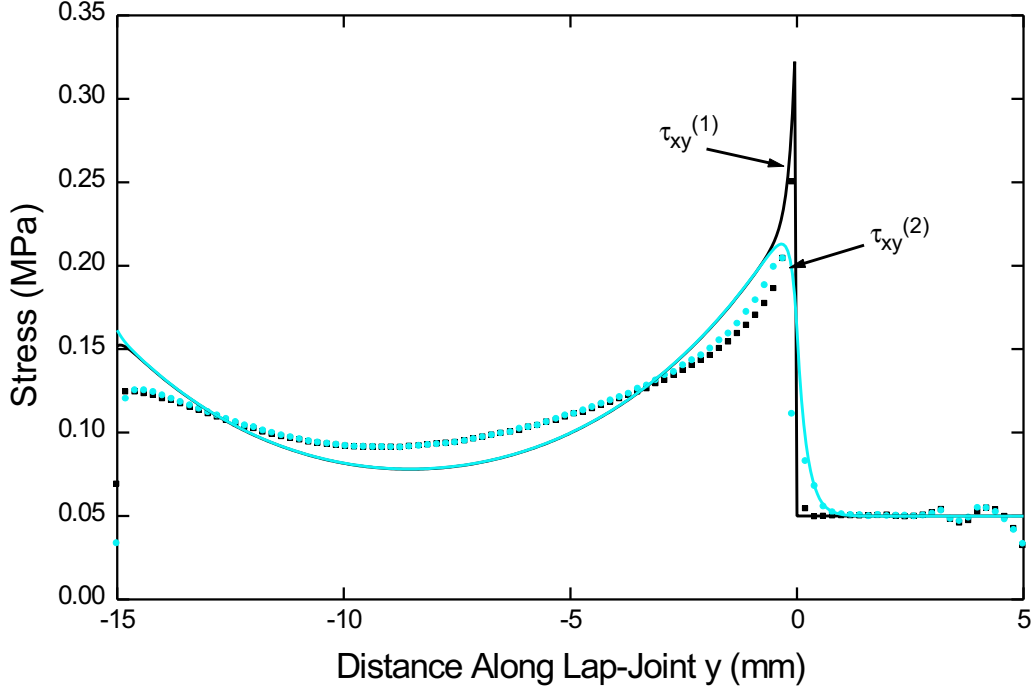


Fig. 11. Normalized shear stresses *vs.* distance along a lap-joint, TGMDA-based epoxy adhesive, solution with hyperbolic shape functions, including constant friction in debond zone ( $\tau_f = 0.05\sigma_0$ ,  $\Delta T = 0$ ).

The vectors  $\vec{T}^0$  and  $\vec{u}$  on loaded surfaces and crack surfaces of the MDLS specimen and their contributions to the surface integral are given in Table II. Here  $\sigma_t$  is the transverse stress, as shown in Fig. 1. Using these results with the crack area  $dA = W da$ ,  $G$  can be recast as:

$$G = \frac{1}{2W} \frac{d}{da} \left[ -\sigma_0 t_1 W \langle v_1(a) \rangle + \sigma_0 t_1 W \langle v_3(a-L) \rangle - \sigma_t L W \langle u_3(t) \rangle \right. \\ \left. + W \int_0^a \tau_f (v_1(t_1, y) - v_2(t_1, y)) dy + \int_V \sigma \alpha \Delta T dV \right] \quad (45)$$

Simplifying the volume integral [16] leads to:

$$G = \frac{1}{2} \frac{d}{da} \left[ -\sigma_0 t_1 \langle v_1(a) \rangle + \sigma_0 t_1 \langle v_3(a-L) \rangle - \sigma_t L \langle u_3(t) \rangle \right. \\ \left. + \int_0^a \tau_f (v_1(t_1, y) - v_2(t_1, y)) dy + L \left( \alpha_y^{(1)} - \alpha_y^{(2)} \right) \Delta T t_1 \overline{\sigma_{yy}^{(1)}} + L \left( \alpha_y^{(3)} - \alpha_y^{(2)} \right) \Delta T t_3 \overline{\sigma_{yy}^{(3)}} \right] \quad (46)$$

where the bars denote phase averaged stresses, calculated as:

$$\overline{\sigma_{yy}^{(i)}} = \int_{V_i} \sigma_{yy}^{(i)} dv = \frac{1}{L} \int_{a-L}^a \langle \sigma_{yy}^{(i)} \rangle dy \quad (47)$$

## 5.2. Approximate Solution

The expression for the energy release rate  $G$  determined by Eq. (46) is exact and depends only on axial stresses and displacements in the three layers. The optimal shear lag analysis is used in this section to get a approximate solution for  $G$ .

### 5.2.1. Calculation of Displacements in the 3 Zones

**Zone I:** In its most general form,

$$\langle v_1 \rangle = \langle v_1(0) \rangle + \int_0^y \langle \varepsilon_{yy}^{(1)} \rangle dy = \langle v_1(0) \rangle + \int_0^y \left( \frac{\sigma_{yy}^{(1)}}{E_y^{(1)}} + \alpha_y^{(1)} \Delta T \right) dy \quad (48)$$

The only approximation here is to ignore contributions of transverse stresses to the axial strain [39]. Taking as a reference for displacements  $\langle v_1(0) \rangle = 0$ , and making use of Eq. (38), one obtains

$$\langle v_1 \rangle = \frac{y}{t_1 E_y^{(1)}} \left( \tau_f (a - \frac{1}{2}y) - \sigma_0 t_1 \right) + \alpha_y^{(1)} \Delta T y \quad (49)$$

and therefore:

$$\langle v_1(a) \rangle = \frac{a}{t_1 E_y^{(1)}} \left( \frac{1}{2} \tau_f a - \sigma_0 t_1 \right) + \alpha_y^{(1)} \Delta T a \quad (50)$$

The edge displacement  $v_1(t_1, y)$  also needs to be calculated. From Eq. (11):

$$v_1(t_1, y) = \langle v_1(y) \rangle + \frac{\tau_f t_1}{G_{xy}^{(1)}} \langle \xi_1 R_1 \rangle = \frac{y}{t_1 E_y^{(1)}} \left( \tau_f (a - \frac{1}{2}y) - \sigma_0 t_1 \right) + \alpha_y^{(1)} \Delta T y + \frac{\tau_f}{G_{xy}^{(1)}} t_1 \langle \xi_1 R_1 \rangle \quad (51)$$

**Zone II:** By a similar analysis:

$$\langle v_2 \rangle = \langle v_2(0) \rangle + \int_0^y \left( \frac{\sigma_{yy}^{(2)}}{E_y^{(2)}} + \alpha_y^{(2)} \Delta T \right) dy \quad (52)$$

With  $\langle \sigma_{yy}^{(2)II} \rangle$  given by Eq. (41):

$$\langle v_2 \rangle = \langle v_2(0) \rangle + \frac{a^{II} (e^{\beta y} - 1)}{\beta E_y^{(2)} t_2} - \frac{b^{II} (e^{-\beta y} - 1)}{\beta E_y^{(2)} t_2} + \tau_f \frac{(y^2 - 2ay)}{2(t_2 + t_3) E_y^{(0)II}} + \alpha_y^{(0)II} \Delta T y \quad (53)$$

To obtain the  $\langle v_2(0) \rangle$  term, the edge displacement  $v_2(t_1, y)$  needs to be calculated first. Again, from Eq. (11), and with accounting for shear stresses on the edges of zone II:

$$v_2(t_1, y) = \langle v_2(y) \rangle - \frac{\tau_{xy}^{(2)II}(y) t_2}{G_{xy}^{(2)}} \langle \xi_2 R_2 \rangle - \frac{\tau_f}{G_{xy}^{(2)}} t_2 \langle \xi_2 L_2 \rangle \quad (54)$$

The continuity of axial displacement between zones I and II at  $y = 0$ :

$$v_2(t_1, 0) = v_1(t_1, 0) \quad (55)$$

yields

$$\langle v_2(0) \rangle + \frac{\tau_{xy}^{(2)}(0)}{G_{xy}^{(2)}} t_2 \langle \xi_2 R_2 \rangle - \frac{\tau_f}{G_{xy}^{(2)}} t_2 \langle \xi_2 L_2 \rangle = \frac{\tau_f}{G_{xy}^{(1)}} t_1 \langle \xi_1 R_1 \rangle \quad (56)$$

and

$$\langle v_2(0) \rangle = \frac{t_2 \langle \xi_2 R_2 \rangle}{G_{xy}^{(2)}} \left( \beta a^{II} - \beta b^{II} - \frac{E_y^{(3)} t_3 \tau_f}{E_y^{(0)II} (t_2 + t_3)} \right) + \frac{\tau_f}{G_{xy}^{(2)}} t_2 \langle \xi_2 L_2 \rangle + \frac{\tau_f}{G_{xy}^{(1)}} t_1 \langle \xi_1 R_1 \rangle \quad (57)$$

Assembling all contributions:

$$v_2(t_1, y) = \frac{t_2 \langle \xi_2 R_2 \rangle}{G_{xy}^{(2)}} \left( \beta a^{II} - \beta b^{II} - \frac{E_y^{(3)} t_3 \tau_f}{E_y^{(0)II} (t_2 + t_3)} + \tau_{xy}^{(2)II}(y) \right) + \frac{\tau_f}{G_{xy}^{(1)}} t_1 \langle \xi_1 R_1 \rangle \quad (58)$$

$$+ \frac{a^{II} (e^{\beta y} - 1)}{\beta E_y^{(2)} t_2} - \frac{b^{II} (e^{-\beta y} - 1)}{\beta E_y^{(2)} t_2} + \frac{\tau_f (y^2 - 2ay)}{2E_y^{(0)II} (t_2 + t_3)} + \alpha_y^{(0)II} \Delta T y$$

The difference of displacements is now:

$$v_1(t_1, y) - v_2(t_1, y) = \frac{y}{t_1 E_y^{(1)}} \left( \tau_f (a - \frac{1}{2}y) - \sigma_0 t_1 \right) + \left( \alpha_y^{(1)} - \alpha_y^{(0)II} \right) \Delta T y - \frac{\tau_f (y^2 - 2ay)}{2(t_2 + t_3) E_y^{(0)II}} \quad (59)$$

$$+ \left( \frac{\beta t_2 \langle \xi_2 R_2 \rangle}{G_{xy}^{(2)}} - \frac{1}{\beta E_y^{(2)} t_2} \right) (a^{II} (e^{\beta y} - 1) - b^{II} (e^{-\beta y} - 1))$$

Integrating this expression between 0 and  $a$  gives:

$$\int_0^a \tau_f (v_1(t_1, y) - v_2(t_1, y)) dy = \tau_f \left\{ \frac{2\tau_f a^3 - 3\sigma_0 t_1 a^2}{6t_1 E_y^{(1)}} + \left( \alpha_y^{(1)} - \alpha_y^{(0)II} \right) \Delta T \frac{a^2}{2} + \frac{\tau_f a^3}{3(t_2 + t_3) E_y^{(0)II}} \quad (60)$$

$$+ \left( \frac{\beta t_2 \langle \xi_2 R_2 \rangle}{G_{xy}^{(2)}} - \frac{1}{\beta E_y^{(2)} t_2} \right) \left[ a^{II} \left( \frac{e^{\beta a} - 1}{\beta} - a \right) + b^{II} \left( \frac{e^{-\beta a} - 1}{\beta} + a \right) \right] \right\}$$

**Zone III:** The last displacements that need to be evaluated in Eq. (46) are  $\langle v_3(a-L) \rangle - \langle v_1(a) \rangle$ . From Eq. (12):

$$\langle v_2 \rangle = \langle v_1 \rangle + \tau_{xy}^{(2)} \frac{t_2 \langle (1 - \xi_2) R_2 \rangle}{G_{xy}^{(2)}} + \tau_{xy}^{(1)} \left[ \frac{t_1 \langle \xi_1 R_1 \rangle}{G_{xy}^{(1)}} + \frac{t_2 \langle (1 - \xi_2) L_2 \rangle}{G_{xy}^{(2)}} \right] \quad (61a)$$

$$\langle v_3 \rangle = \langle v_2 \rangle + \tau_{xy}^{(2)} \left[ \frac{t_3 \langle (1 - \xi_3) L_3 \rangle}{G_{xy}^{(3)}} + \frac{t_2 \langle \xi_2 R_2 \rangle}{G_{xy}^{(2)}} \right] + \tau_{xy}^{(1)} \frac{t_2 \langle \xi_2 L_2 \rangle}{G_{xy}^{(2)}} \quad (61b)$$

and, by eliminating  $\langle v_2 \rangle$  results in:

$$\langle v_3 \rangle = \langle v_1 \rangle + \tau_{xy}^{(2)} \left[ \frac{t_3 \langle (1 - \xi_3) L_3 \rangle}{G_{xy}^{(3)}} + \frac{t_2 \langle \xi_2 R_2 \rangle}{G_{xy}^{(2)}} + \frac{t_2 \langle (1 - \xi_2) R_2 \rangle}{G_{xy}^{(2)}} \right] \quad (62)$$

$$+ \tau_{xy}^{(1)} \left[ \frac{t_1 \langle \xi_1 R_1 \rangle}{G_{xy}^{(1)}} + \frac{t_2 \langle (1 - \xi_2) L_2 \rangle}{G_{xy}^{(2)}} + \frac{t_2 \langle \xi_2 L_2 \rangle}{G_{xy}^{(2)}} \right]$$

It follows from Eq. (48) that:

$$\langle v_3(a-L) \rangle - \langle v_1(a) \rangle = \int_a^{a-L} \left( \frac{\langle \sigma_{yy}^{(1)} \rangle}{E_y^{(1)}} + \alpha_y^{(1)} \Delta T \right) dy \quad (63)$$

$$+ \left[ \frac{t_1 \langle \xi_1 R_1 \rangle}{G_{xy}^{(1)}} + \frac{t_2 \langle (1 - \xi_2) L_2 \rangle}{G_{xy}^{(2)}} + \frac{t_2 \langle \xi_2 L_2 \rangle}{G_{xy}^{(2)}} \right] \tau_{xy}^{(1)} (a-L)$$

$$+ \left[ \frac{t_3 \langle (1 - \xi_3) L_3 \rangle}{G_{xy}^{(3)}} + \frac{t_2 \langle \xi_2 R_2 \rangle}{G_{xy}^{(2)}} + \frac{t_2 \langle (1 - \xi_2) R_2 \rangle}{G_{xy}^{(2)}} \right] \tau_{xy}^{(2)} (a-L)$$

Making use of the phase-averaged stress definition (Eq. (47)):

$$\begin{aligned} \langle v_3(a-l) \rangle - \langle v_1(a) \rangle &= -L \frac{\overline{\sigma_{yy}^{(1)}}}{E_y^{(1)}} - \alpha_y^{(1)} \Delta T L + \left[ \frac{t_1 \langle \xi_1 R_1 \rangle}{G_{xy}^{(1)}} + \frac{t_2 \langle (1-\xi_2) L_2 \rangle}{G_{xy}^{(2)}} + \frac{t_2 \langle \xi_2 L_2 \rangle}{G_{xy}^{(2)}} \right] \tau_{xy}^{(1)}(a-L) \\ &\quad + \left[ \frac{t_3 \langle (1-\xi_3) L_3 \rangle}{G_{xy}^{(3)}} + \frac{t_2 \langle \xi_2 R_2 \rangle}{G_{xy}^{(2)}} + \frac{t_2 \langle (1-\xi_2) R_2 \rangle}{G_{xy}^{(2)}} \right] \tau_{xy}^{(2)}(a-l) \end{aligned} \quad (64)$$

### 5.2.2. Phase Averaged Stresses

Combining all displacement results, the energy release rate can be written as:

$$\begin{aligned} G &= \frac{1}{2} \frac{d}{da} \left[ \sigma_0 t_1 \left( -L \frac{\overline{\sigma_{yy}^{(1)}}}{E_y^{(1)}} - \alpha_1 \Delta T L + \left[ \frac{t_1 \langle \xi_1 R_1 \rangle}{G_{xy}^{(1)}} + \frac{t_2 \langle (1-\xi_2) L_2 \rangle}{G_{xy}^{(2)}} + \frac{t_2 \langle \xi_2 L_2 \rangle}{G_{xy}^{(2)}} \right] \tau_{xy}^{(1)}(a-L) \right. \right. \\ &\quad \left. \left. + \left[ \frac{t_3 \langle (1-\xi_3) L_3 \rangle}{G_{xy}^{(3)}} + \frac{t_2 \langle \xi_2 R_2 \rangle}{G_{xy}^{(2)}} + \frac{t_2 \langle (1-\xi_2) R_2 \rangle}{G_{xy}^{(2)}} \right] \tau_{xy}^{(2)}(a-L) \right) \right. \\ &\quad \left. - \sigma_t L \langle u_3(t) \rangle + \tau_f \left\{ \frac{2\tau_f a^3 - 3\sigma_0 t_1 a^2}{6t_1 E_y^{(1)}} + (\alpha_y^{(1)} - \alpha_y^{(0)II}) \Delta T \frac{a^2}{2} + \frac{\tau_f a^3}{3(t_2 + t_3) E_y^{(0)II}} \right. \right. \\ &\quad \left. \left. + \left( \frac{\beta t_2 \langle \xi_2 R_2 \rangle}{G_{xy}^{(2)}} - \frac{1}{\beta E_y^{(2)} t_2} \right) \left[ a^{II} \left( \frac{e^{\beta a} - 1}{\beta} - a \right) + b^{II} \left( \frac{e^{-\beta a} - 1}{\beta} + a \right) \right] \right\} \right. \\ &\quad \left. + L \left( \alpha_y^{(1)} - \alpha_y^{(2)} \right) \Delta T t_1 \overline{\sigma_{yy}^{(1)}} + L \left( \alpha_y^{(3)} - \alpha_y^{(2)} \right) \Delta T t_3 \overline{\sigma_{yy}^{(3)}} \right] \end{aligned} \quad (65)$$

This key terms needed are the phase-averaged axial stresses that are obtained from:

$$\overline{\sigma_{yy}^{(1)}} = \frac{1}{L} \left( \int_{a-L}^0 \langle \sigma_{yy}^{(1)III} \rangle dy + \int_0^a \langle \sigma_{yy}^{(1)I} \rangle dy \right) \quad (66)$$

$$\overline{\sigma_{yy}^{(3)}} = \frac{1}{L} \left( \int_{a-L}^0 \langle \sigma_{yy}^{(3)III} \rangle dy + \int_0^a \langle \sigma_{yy}^{(3)II} \rangle dy \right) \quad (67)$$

The following integrals are needed:

$$\int_0^a \langle \sigma_{yy}^{(1)I} \rangle dy = \frac{\tau_f}{2t_1} a^2 - \sigma_0 a \quad (68)$$

The exponential coefficients and eigenvalues  $a_i^k, b_i^k, \beta$  and  $\lambda_i$  do not depend upon the axial coordinate  $y$ , which makes it possible to integrate the stresses; the result is

$$\begin{aligned} \int_0^a \langle \sigma_{yy}^{(3)II} \rangle dy &= \frac{1}{t_3} \left\{ \frac{a^{II} (1 - e^{\beta a})}{\beta} + \frac{b^{II} (e^{-\beta a} - 1)}{\beta} \right. \\ &\quad \left. + E_y^{(3)} t_3 a \left[ (\alpha_y^{(0)II} - \alpha_y^{(3)}) \Delta T - \frac{\tau_f a}{2E_y^{(0)II} (t_2 + t_3)} \right] \right\} \end{aligned} \quad (69)$$

$$\begin{aligned}
\int_{a-L}^0 \langle \sigma_{yy}^{(1)III} \rangle dy &= \left[ a_1^{III} \left( 1 - e^{\lambda_1(a-L)} \right) + b_1^{III} \left( e^{-\lambda_1(a-L)} - 1 \right) \right] \frac{\omega_{2,1}}{\lambda_1^2 t_1} \\
&+ \left[ a_2^{III} \left( 1 - e^{\lambda_2(a-L)} \right) + b_2^{III} \left( e^{-\lambda_2(a-L)} - 1 \right) \right] \frac{\omega_{2,1}}{\lambda_2^2 t_1} \\
&+ E_y^{(1)} (a-L) \left( \frac{-t_1 \sigma_0}{t E_y^{(0)}} + \left( \alpha_y^{(0)} - \alpha_y^{(1)} \right) \Delta T \right)
\end{aligned} \tag{70}$$

and

$$\begin{aligned}
\int_{a-L}^0 \langle \sigma_{yy}^{(3)III} \rangle dy &= \left[ a_1^{III} \left( e^{\lambda_1(a-L)} - 1 \right) + b_1^{III} \left( 1 - e^{-\lambda_1(a-L)} \right) \right] \frac{\omega_{2,1}}{\lambda_1^2 t_3} \\
&+ \left[ a_2^{III} \left( e^{\lambda_2(a-L)} - 1 \right) + b_2^{III} \left( 1 - e^{-\lambda_2(a-L)} \right) \right] \frac{\omega_{2,2}}{\lambda_2^2 t_3} \\
&+ E_y^{(3)} (a-L) \left( \frac{-t_1 \sigma_0}{t E_y^{(0)}} + \left( \alpha_y^{(0)} - \alpha_y^{(3)} \right) \Delta T \right)
\end{aligned} \tag{71}$$

The final energy release rate is found by substituting Eqs (68)–(71) into Eq. (65) and differentiating with respect to crack length  $a$ . Because the constants  $a_i^k$  and  $b_i^k$  are functions of  $a$ , the final differentiation step must be done numerically but the calculations are straightforward.

### 5.3. Results

Figure 12 plots the energy release rate  $G$  calculated from the model (solid curves) compared to that obtained by FEA (symbols), with and without internal stresses, and for various friction stresses. The calculations shown were obtained for a fixed value of  $\sigma_0 = 50$  MPa. For a friction stress of  $\tau_f = 0$ , the energy release rate increases rapidly to about 25 kJ/m<sup>2</sup> and then continues to increase, albeit slowly, to 30 kJ/m<sup>2</sup>. Because  $G$  increases with crack length, the prediction is that crack growth, once started, will be unstable until the end of the specimen. The situation changes dramatically when friction is added. When  $\tau_f$  is not zero, the energy release rate rises to maximum for a certain crack length, and then decreases. In experiments, the prediction is that the crack will rapidly propagate to a length corresponding to the maximum  $G$ . Thereafter, because  $G$  decreases with crack length, the load will have to be increased to propagate the crack. In other words, friction stabilizes the crack propagation.

The shear-lag calculations agree very well with FEA at long crack length ( $a > 3$  mm), but agree less well at shorter crack length. In particular, the maximum in  $G$  when there is friction, is at a much shorter crack length in the shear-lag analysis than in the FEA analysis. The shear-lag analysis was derived from a shear-lag stress analysis that ignores all singularities in the stress state. The energy release rate was derived from a derivative of this stresses in this analysis. Such a derivative analysis will be accurate whenever the effects of the singularity are small or whenever the contribution of the singularities is a constant. When the effect is a constant, it will drop out in the differentiation step. Based on the results in Fig. 12 we claim that the singular effects at the crack tip are a constant provided the crack tip is not too close to the start of the specimen. In other words, the shear-lag analysis is accurate provided  $a$  is not too short. When  $a$  is too short, the crack tip complexities will be influenced by the free surface. The shear-lag analysis does not account for this effect and thus the accuracy is lowered. Similar conclusions were reached in the analysis of debond growth and the fiber-matrix interface in the microbond specimen where a shear-lag analysis was shown to agree with FEA results provided the debond crack tip was not too close to either end of the specimen [44].

The effect of internal stresses, represented by the difference between the upper and lower curves obtained for a same friction stress but different  $\Delta T$ , agrees very well with FEA calculations. This agreement follows because the approximation of average axial stresses by shear lag is very accurate, and because  $\overline{\sigma_{yy}^{(1)}}$  and  $\overline{\sigma_{yy}^{(3)}}$  dominate the internal stress response of the system at long crack length. The accurate description of internal stress effects works for all values of friction stress.

The model accuracy is influenced by the choice of shape functions, and it is possible to improve the results by adjusting them. Unfortunately, this approach only provides a partial solution to any disagreements

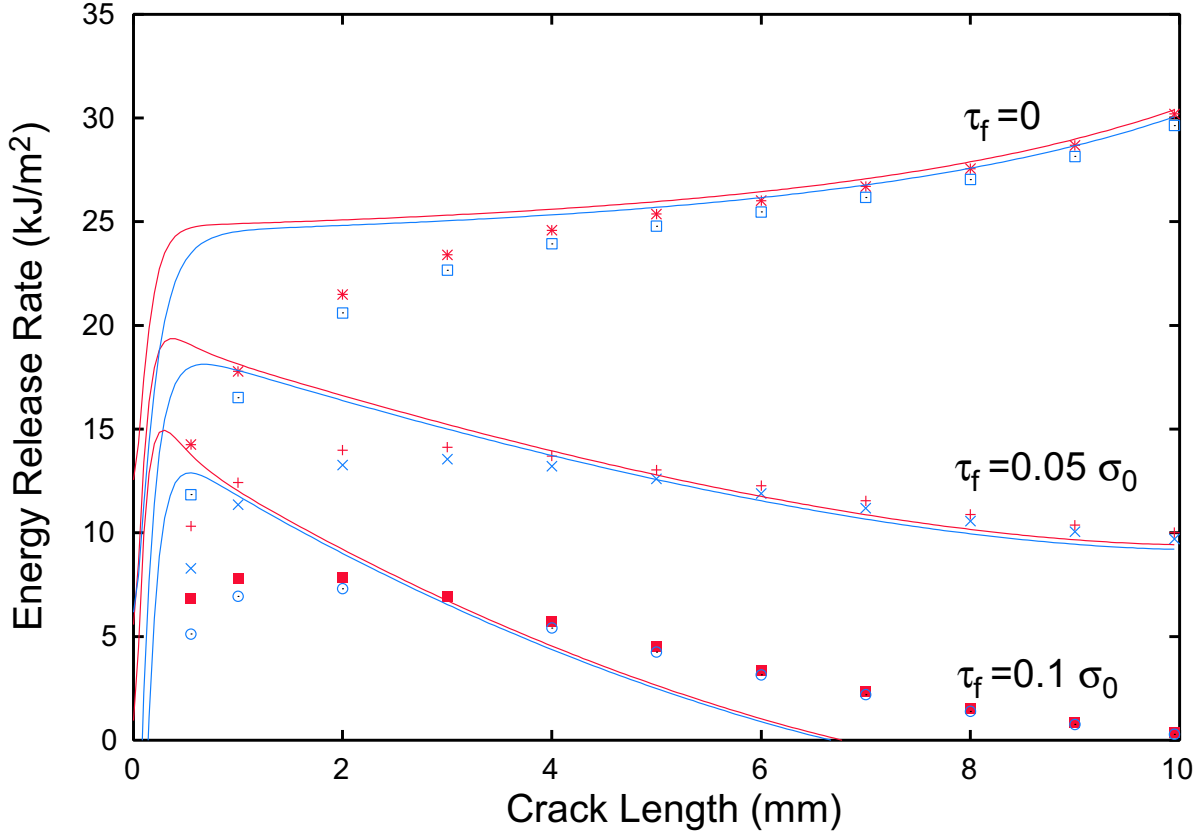


Fig. 12. Energy release rate of a debonding interface: model (solid curves) vs. FEA results (symbols), for various coefficients of friction and internal stress levels. For each friction coefficient, the upper curve has  $\Delta T = -100^\circ\text{C}$ , and the lower curve  $\Delta T = 0$ .

mentioned above. Another approach could be to fix the shape functions as linear, but to increase the number of layers. In other words, each physical layer could be divided into additional layers and the resulting problem analyzed by multilayer shear-lag methods [39]. The model's accuracy would benefit from this approach, but the calculations would require more numerical work.

To conclude, the model is applicable provided the friction stress is between 0 and  $0.05\sigma_0$ , and the crack length is greater than about 3 mm. The friction stress has a larger influence on the energy release rate than the internal stress level, and it should therefore be determined accurately in an experimental study.

## 6. Conclusions

This study introduced a new geometry for a lap-shear test, the modified double lap shear (MDLS) specimen. The stress state in the MDLS specimen, including residual stresses, was obtained from a modified shear-lag theory, extended to account for non-perfect interfaces and also local variations in the adhesive mechanical behavior. Two alternative theories were devised to interpret the test results, namely the interfacial shear strength approach and the energy release rate approach. Stress shape functions were used to refine the stress analysis, and average displacements were calculated accordingly. The local stress states and the approximate energy release rate were shown to compare well to FEA results. For energy release rate, it was shown that the model is valid provided the crack length is larger than a certain value. Also, the frictional stress greatly influences the value of  $G$ ; thus friction greatly influences crack growth and must be well understood before interpreting any experimental results. The MDLS specimen was analyzed with a generic multilayered theory. This theory could be applied to other systems such as the modelling of transverse nano-indentation of multilayered systems.

## 7. Acknowledgements

The authors are indebted to the Swiss National Science Foundation for financial support. One author (J. A. Nairn) was supported by a grant from the Mechanics of Materials program at the National Science Foundation (CMS-9713356).

## REFERENCES

1. L.J. Hart-Smith. Bonded-bolted composite joints. In *AIAA/ASME/ASCE/AHS 25th Structures, Structural Dynamics and Materials Conference*, pages 1–11, Palm Springs, California, May 14-16 1984. ASTM.
2. L.J. Hart-Smith. Design and analysis of bolted and riveted joints in fibrous composite structures. In *International Symposium on Joining and Repair of Fibre-Reinforced Plastics*, pages 1–15, London, Sept. 10-11 1986. Imperial College.
3. Stress Analysis DE-Vol. 100, Reliability, Failure Prevention Aspects of Adhesive, Rubber Components Bolted Joints, and Composite Springs, editors. *Stress Analysis And Strength Evaluation of Single-Lap Band Adhesive Joints Subjected to External Bending Moments*. ASME, ASME, 1998.
4. A.N. Gent and E.A. Meinecke. Compression, bending, and shear of bonded rubber blocks. *Polym. Engin. Sci.*, 10:48–53, 1970.
5. A.N. Gent. Fracture mechanics of adhesive bonds. In *The Rubber Division*, pages 202–212, Denver, Colorado, Oct. 9-12 1973. Am. Chem. Soc.
6. S. Mall and K.M. Liechti, editors. *On Three Dimensional Stress States in Adhesive Joints*, Chicago, Illinois, Nov. 17- Dec. 2 1988. The American Society of Mechanical Engineers, The Winter Annual Meeting of the American Society of Mechanical Engineers.
7. S.R. Pagano and N.J. Soni. *Models for Studying Free-Edge Effects*, volume 5 of *Composite Materials Series, R.B. Pipes Ed.*, chapter 1, pages 1–68. Elsevier Science Publishers, 1989.
8. ASTM D 1002-94. *Standard Test Method for Apparent Shear Strength of Single-Lap-Joint Adhesively Bonded Metal Specimens by Tension Loading*, 1994.
9. ASTM D 3528 96. *Standard Test Method for Strength Properties of Double Lap Shear Adhesive Joints by Tension Loading*, 1996.
10. O. Volkersen. Die nietkraftverteilung in zugbeanspruchten nietverbindungen mit konstanten laschenquerschnitten. *Luftfahrtforschung*, 15:41–47, 1938.
11. M. Goland and E. Reissner. The stresses in cemented joints. *J. Appl. Mech.*, 11:A17–A27, 1944.
12. B. Broughton and M. Gower. Preparation and Testing of Adhesive Joints. Measurement Good Practice Guide 47, National Physical Laboratory, Teddington, Middlesex, United Kingdom, TW11 0LW, 2001.
13. H. Chai and M.Y.M. Chiang. A crack propagation criterion based on local shear strain in adhesive bonds subjected to shear. *J. Mech. Phys. Solids*, 44:1669–1689, 1996.
14. G.P. Anderson and K.L. Devries. *Analysis of Standard Bond-Strength Tests*, volume 6, chapter 3, pages 55–121. Marcel Dekker, Inc., New York and Basel, 1989.
15. P.R. Borgmeier and K.L. Devries. A fracture mechanics analysis of the effects of tapering adherends on the strength of adhesive lap joints. *J. Adhesion Sci. Technol.*, 7(9):967–986, 1993.
16. J.A. Nairn. Exact and variational theorems for fracture mechanics of composites with residual stresses, traction-loaded cracks, and imperfect interfaces. *Int. J. Fract.*, 105:243–271, 2000.
17. F. Erdogan, F. Delale, and M.N. Aydinoglu. Stresses in adhesively bonded joints: A closed-form solution. *J. Compos. Mater.*, 15:249–271, 1981.
18. W.C. Carpenter. A comparison of numerous lap joint theories for adhesively bonded joints. *J. Adhesion*, 35:55–73, 1991.
19. M.Y.M. Chiang and H. Chai. Plastic deformation analysis of cracked adhesive bonds loaded in shear. *Int. J. Solids Structures*, 31:2477–2490, 1994.
20. M.Y.M. Chiang and H. Chai. A finite element analysis of interfacial crack propagation based on local shear, part I - near tip deformation. *Int. J. Solids Structures*, 00:14, 1997.
21. H. Chai and M.Y.M. Chiang. Finite element analysis of interfacial crack propagation based on local shear, part II - fracture. *Int. J. Solids Structures*, 00:14, 1997.

22. D.B. Bogy. Edge-bonded dissimilar orthogonal elastic wedges under normal and shear loading. *J. Appl. Mech.*, (Sept.):460–466, 1968.
23. J. Dundurs. Edge-bonded dissimilar orthogonal elastic wedges under normal and shear loading. *J. Appl. Mech.*, (September):650–652, 1969.
24. A. Gilibert and Y. Rigolot. Analyse asymptotique des assemblages collés à double recouvrement sollicités au cisaillement en traction. *Journal de Mécanique appliquée*, 3:341–372, 1979.
25. K.L. DeVries and P.R. Borgmeier. *Fracture mechanics analyses of the behavior of adhesion test specimens*. VSP, 1998.
26. D.-A. Mendels, Y. Leterrier, and J.-A. E. Månson. The influence of internal stresses on the microbond test 1: Theoretical analysis. *J. Compos. Mater.*, in press, 2001.
27. D.-A. Mendels, Y. Leterrier, and J.-A. E. Månson. The influence of internal stresses on the microbond test 2: Experimental interpretation including the effect of relaxation. *J. Compos. Mater.*, Accepted, 2001.
28. L.J. Hart-Smith. Effects of flaws and porosity on strength of adhesive-bonded joints. Technical Report F33615-80-C-5092, PR No. 5, Douglas Aircraft Company, 3855 Lakewood Boulevard, Long Beach, California 90846, 1981.
29. M.L.L. Gilibert, Y. Klein, and A. Rigolot. Modélisation d'un composite plan en présence de micro-défauts. Technical Report 207, ENSTA, 1986.
30. L.J. Hart-Smith. Adhesive layer thickness and porosity criteria for bonded joints. Technical Report F33615-80-C-5092, PR No. 3, Douglas Aircraft Company, 3855 Lakewood Boulevard, Long Beach, California 90846, 1981.
31. D.-A. Mendels, J. Wolfrath, S.A. Page, J.-A. E. Månson, and C. Galiotis. A modified double lap-shear test: Part 2, determination of local stress state by means of raman spectroscopy. *Int. J. Adh. Adhes.*, to be Submitted, 2000.
32. S.A. Page, D.-A. Mendels, L. Boogh, and J.-A.E. Månson. A modified double lap-shear test: Part 3, the influence of internal stresses on practical adhesion. *Int. J. Adh. Adhes.*, to be Submitted, 2001.
33. D.-A. Mendels, Y. Leterrier, and J.-A.E. Månson. A modified double lap-shear test: Part 4, the influence of physical aging on practical adhesion. *Int. J. Adh. Adhes.*, to be Submitted, 2001.
34. D.-A. Mendels. A modified double lap shear test: Part 5, interfacial crack propagation in cross-ply laminates subjected to static or cyclic loading. *Int. J. Adh. Adhes.*, to be Submitted, 2001.
35. S.A. Page, D.-A. Mendels, L. Boogh, and J.-A.E. Månson. Influence of the internal stress state on the adhesive performance of epoxy films determined by a new bonded-joint test. Brighton, UK, June 4-7 2000. IOM Publ. ltd.
36. S.A. Page, L. Boogh, and J.-A.E. Månson. Process and material tailoring for internal stress control. *J. Appl. Polym. Sci.*, submitted, 2000.
37. D.-A. Mendels, Y. Leterrier, and J.-A.E. Månson. A stress transfer model for single fibre and platelet composites. *J. Compos. Mater.*, 33:1525–1544, 1999.
38. D.-A. Mendels, Y. Leterrier, and J.-A.E. Månson. Property modelling of epoxy laminates including thermal stresses and relaxation behaviour upon physical aging. In A.H. Cardon, editor, *DURACOSYS'99*, Brussels, July 12-14 1999. Balkema.
39. J.A. Nairn and D.-A. Mendels. On the use of planar shear-lag methods for stress-transfer analysis of multilayered composites. *Mech. Mater.*, 33:335–362, 2001.
40. D.-A. Mendels, S.A. Page, Y. Leterrier, and J.-A.E. Månson. A modified double lap-shear test as a mean to measure intrinsic properties of adhesive joints. Brighton, UK, June 4-7 2000. IOM Publ. ltd.
41. D.-A. Mendels. Analysis of the single-fibre fragmentation test. NPL Report MATC (A)17, National Physical Laboratory, Teddington, Middlesex, United Kingdom, TW11 0LW, 2001.
42. M.J. Lodeiro, S. Maugdal, L.N. McCartney, R. Morrell, and B. Roebuck. Critical review of interface methods for composites. NPL Report CMMT(A)101, National Physical Laboratory, 1998.
43. L.N. McCartney. Stress transfer mechanics for systems of transverse isotropic concentric cylinders, I-basic theory. in preparation, 2001.
44. C.H. Liu and J.A. Nairn. Analytical Fracture Mechanics of the Microbond Test Including the Effects of Friction and Thermal Stresses. *J. of Adhes. and Adhesives*, 19:59–70, 1999.